Tidal and Atmospheric Forcing of the Upper Ocean in the Gulf of California
1.   Sea Surface Temperature Variability

Cynthia A. Paden[1]

Center for Coastal Studies, Scripps Institution of Oceanography, La Jolla, California

Mark R. Abbott

College of Oceanography, Oregon State University, Corvallis

Clinton D. Winant

Center for Coastal Studies, Scripps Institution of Oceanography, La Jolla, California

Two years of satellite infrared imagery (1984–1986) are used to examine the sea surface temperature (SST) variability in the northern Gulf of California. Empirical orthogonal functions (EOFs) of the temporal and spatial SST variance for 20 monthly mean images show that the dominant SST patterns are generated by spatially varying tidal mixing in the presence of seasonal heating and cooling. These patterns are modified in the fall and winter when shelf temperatures south of Tiburon Island cool in response to upwelling-favorable winds. These same winds bring cold, dry air from off the continental United States, causing local cooling of the shallow northern shelf. During the rest of the year, the broad, shallow shelves are warmer than offshore. The seasonally reversing temperature patterns are consistent with recent hydrographic observations which show a cyclonic surface circulation in the summer and a weaker anticyclonic circulation during the rest of the year. Atmospheric forcing of the northern gulf appears to occur over large spatial scales. Area-averaged SSTs for the Guaymas Basin, island region, and northern basin show significant fluctuations which are highly correlated. These fluctuations in SST correspond to similar fluctuations in the air temperature which are related to synoptic weather events over the gulf. During periods of particularly low wind speeds, the air temperature over the gulf increases dramatically. By afternoon, intense heating of the sea surface results in the appearance of warm SST anomalies in the satellite data. These SSTs are approximately 2°C warmer than surrounding SSTs and most likely occur as a result of a spatially varying wind field. A regression analysis of the SST relative to the fortnightly tidal range shows that tidal mixing occurs over the sills in the island region as well as on the shallow norther shelf. Mixing over the sills, however, occurs as a result of large breaking internal waves or internal hydraulic jumps which mix water over the upper 300–500 m. This mixing pumps heat away from the surface, deep into the water column, thereby maintaining the cool SSTs. Since mixing occurs over greater depths in the island region, the temperatures there are much colder than those generated by tidal mixing on the shallow shelves, resulting in the persistent pool of cool water evident in the satellite data. This cooler water is mixed horizontally by the basin-scale circulation, lowering the SSTs over much of the northern gulf. These reduced SSTs have a large impact on the surface heat flux by lowering the saturation vapor pressure of the air. As a result, the amount of heat lost to the atmosphere through the latent or evaporative heat flux is reduced. This may explain why the Gulf of California gains heat on an annual average rather than losing heat as occurs in the Mediterranean and Red seas where tidal mixing is not significant.

1.   Introduction

The Gulf of California, unlike the Mediterranean and Red seas, gains heat on an annual average. This is contrary to what is usually expected for evaporative basins and to early estimates of the heat flux based on coastal atmospheric data [*Roden and Emilsson*, 1979]. Hydrographic estimates of the advective heat transport for the northern Gulf of California [*Bray*, 1988a] show a net export of heat in the upper 500 m implying a net gain from the atmosphere of approximately 22 W m^{-2}. A recent estimate of the net surface heat flux from atmospheric data and historical sea surface temperatures

(SSTs) [*Lavin and Organista*, 1988] suggests a net gain of approximately 80 W m^{-2} in the shallow northern basin, consistent with the hydrographic results. The heat gain, in conjunction with evaporation, produces warm, relatively saline surface waters which flow out of the gulf in exchange for colder, fresher water at depth [*Bray*, 1988a]. This circulation is opposite to that observed in the Mediterranean and Red seas, where a warm, relatively fresh inflow at the surface compensates for the cold, saline outflow at depth.

The outflowing water mass in the Gulf of California is substantially modified as a result of vigorous tidal mixing [*Bray*, 1988b]. This mixing is also believed to be responsible for the consistently cooler surface temperatures observed in the midriff island region of the gulf [*Roden*, 1958; *Badan-Dangon et al.*, 1985]. Since the sea surface temperature is a determining factor in the exchange of heat between the ocean and atmosphere, its modification by processes such as tidal mixing, upwelling, wind mixing, and advection can be

---

[1]Now at College of Oceanography, Oregon State University, Corvallis.

fundamental to the net gain of heat by the gulf. Since density in the gulf is primarily a function of temperature [*Bray*, 1988a], SST patterns can also be used to infer the surface density field. In this paper we examine the temporal and spatial patterns of the SST variability in an attempt to understand the mechanisms which establish those patterns and lead to the observed circulation in the Gulf of California.

In recent years, satellite infrared imagery has proven to be a powerful tool in the study of upper ocean processes. This has been particularly true for studies of coastal upwelling [*Kelly*, 1985; *Flament et al.*, 1985] and tidal mixing fronts [*Simpson and Hunter*, 1974; *Loder and Greenberg*, 1986], where strong temperature gradients are generated at the surface between well-mixed waters at the coast and stratified waters offshore. Since both processes produce relatively homogeneous water columns, changes in temperature at the surface will be correlated with changes throughout the upper layer. These changes in SST can then be related to variability in the forcing, permitting a more synoptic view of the ocean response than can be obtained from in situ hydrographic measurements alone.

Satellite infrared images were collected from March 1984 through February 1986 corresponding to the time period of a thermohaline circulation study. This study was part of a joint field program carried out by investigators from Scripps Institution of Oceanography and Centro de Investigación Científica y de Educación Superior de Ensenada to study the circulation in the northern Gulf of California. In addition to the hydrographic surveys, moored current and temperature measurements were made on both shelves in the Guaymas Basin, and meteorological variables were measured at several portable weather stations located throughout the study area.

A brief background of the Gulf of California is presented in section 2 with a description of the data and data processing techniques in section 3. In section 4 the seasonal variability of the SST is described using empirical orthogonal functions. In section 5 the short-term SST variability is examined and related to tidal and atmospheric forcing. In section 6 the results are summarized and the role of tidal mixing in the net gain of heat by the gulf is discussed.

2. BACKGROUND

The Gulf of California is a marginal sea of the Pacific Ocean located between the Mexican mainland and the Baja California peninsula (Figure 1). It is approximately 1000 km long and 150 km wide and is composed of three regions distinguished by their hydrographic and bathymetric characteristics. In the south, the gulf consists of a series of deep basins (1000–3000 m) which are in open communication with the Pacific Ocean. At the upper end of this region lies the Guaymas Basin, which is separated from the relatively shallow northern basin (average depth of 200 m) by the complex bathymetry of the midriff island region near 29°N. These islands form several channels, the most prominent being along the western side of the gulf (the Ballenas and Salsipuedes channels), where the depth exceeds 1000 meters. Sills located at the southern end of the Salsipuedes Channel (Salsipuedes Sill) and in the adjacent San Esteban Channel (San Esteban Sill) isolate deep waters of the Guaymas Basin and the northern basin below 500 m [*Bray*, 1988a, b]. A constriction or sill is also present in the Ballenas

Channel. The study area includes the northern basin, the island region and the Guaymas basin, all of which will be referred to as the "northern gulf."

Winds are polarized along the axis of the gulf owing to the presence of a continuous chain of mountains on the Baja California peninsula. These same mountains isolate the gulf from the marine influence of the Pacific Ocean, making the climate of the gulf more continental than oceanic [*Alvarez-Borrego*, 1983]. Winds blowing from the southeast during the summer advect warm, moist tropical air into the gulf. These winds are relatively weak (2–5 m/s) and quite variable in space. During the rest of the year winds blow off the continental United States bringing cool, dry air over the northern gulf. These winds are stronger (8–12 m/s) and are coherent over the study area [*Merrifield and Winant*, 1989; *Badan-Dangon et al.*, 1991].

Geostrophic current estimates from hydrographic sections across the Guaymas Basin and the northern basin indicate that the surface circulation in the gulf is cyclonic during the summer, with a weaker anticyclonic circulation during the rest of the year [*Bray*, 1988a]. Integrated transports show a net inflow primarily between 250 and 500 m, outflow between 50 and 250 m, and a net surface transport in the direction of the seasonal winds [*Bray*, 1988a]. Moored measurements of the shelf currents on both sides of the Guaymas Basin also show a seasonally reversing circulation, with a mean flow corresponding to the seasonal winds [*Merrifield and Winant*, 1989].

The gulf is resonant to the semidiurnal tide with tidal ranges as large as 10 m at its northern end [*Roden and Groves*, 1959]. These ranges produce large tidal currents, especially in the narrow channels of the island region, where currents as large as 3 m/s have been observed [*Roden*, 1964]. Calculations of energy dissipation indicate that over 80% of the tidal energy entering the gulf is dissipated north of the Guaymas Basin [*Filloux*, 1973], resulting in a virtual amphidrome over the Baja California peninsula [*Hendershott and Speranza*, 1971]. Most of this energy is lost through bottom friction [*Stock*, 1976], with an estimated 10% dissipated through the generation of internal waves at the sills [*Fu and Holt*, 1984].

3. SATELLITE DATA

A total of 197 afternoon passes from the NOAA 7 and NOAA 9 polar-orbiting satellites were processed for the period March 1984 through February 1986 (Tables 1a and 1b). The afternoon pass occurs at approximately 1400 LT and was chosen for the analysis due to the prevalence of low clouds or fog at other times of the day. Images selected for the analysis were relatively cloud-free and had zenith view angles of less than 53° [*McClain et al.*, 1985]. The data were collected by the Scripps Satellite Oceanography Facility (SSOF) and processed at the Jet Propulsion Laboratory in Pasadena, California, using software developed at the University of Miami by O. Brown and R. Evans [see *Cornillon and Stramma*, 1985].

SSTs were estimated using the Multi-Channel Sea Surface Temperature (MCSST) algorithms for the daytime NOAA 7 and NOAA 9 advanced very high resolution radiometer (AVHRR) data [*McClain et al.*, 1985; R. Evans, personal communication, 1988]. These SST products have a global bias and rms difference of −0.1°C and 0.5°C when compared

BATHYMETRY OF THE NORTHERN GULF PROVINCE
BATHYMETRIC MAPS OF THE GULF OF CALIFORNIA

0   50 km

CD - Colorado River Delta
AB - Adair Bay
JB - San Jorge Bay
BC - Ballenas Channel
SC - Salsipuedes Channel
SS - Salsipuedes Sill
SF - San Francisquito Bay
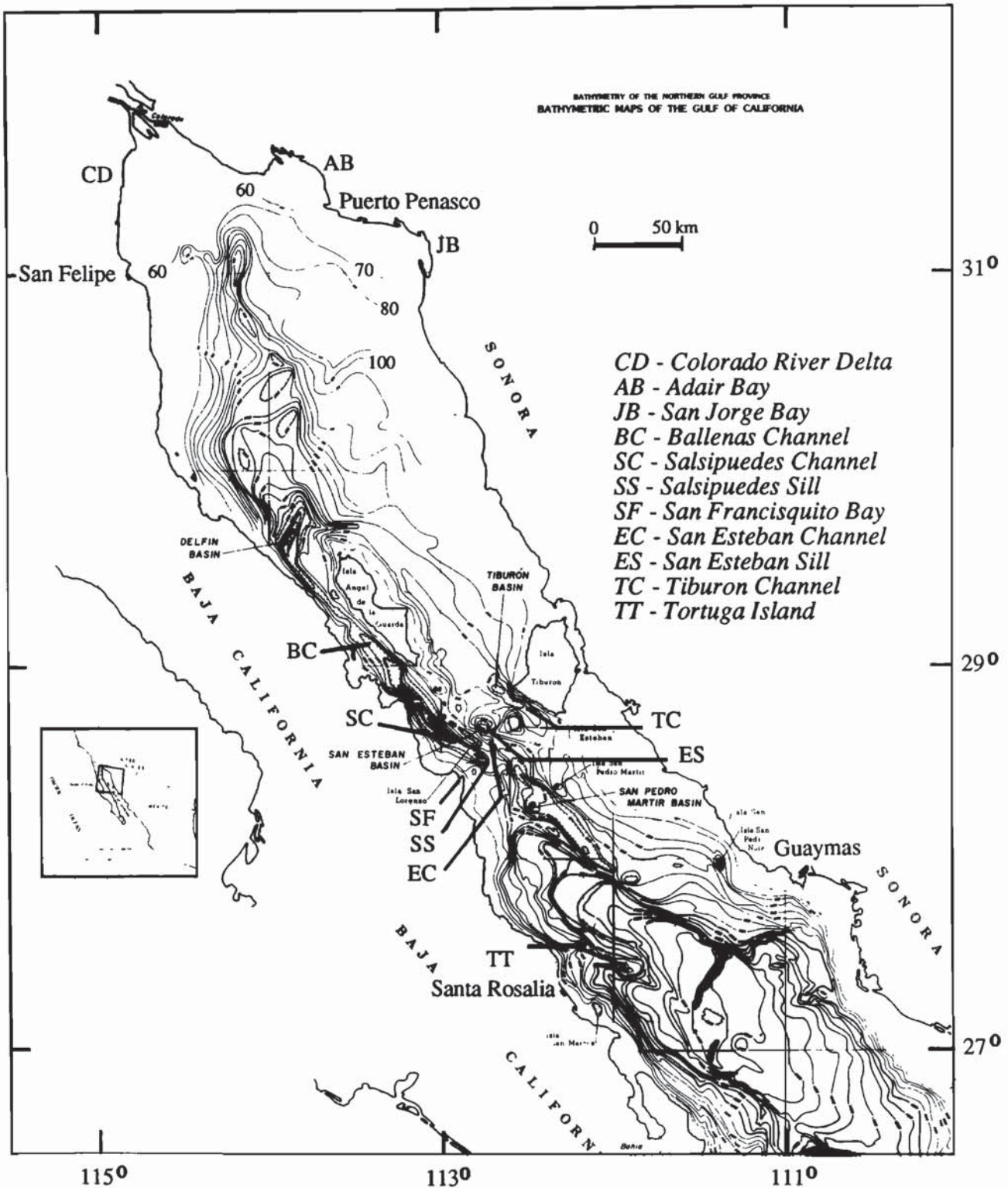EC - San Esteban Channel
ES - San Esteban Sill
TC - Tiburon Channel
TT - Tortuga Island

Fig. 1.   Map of the Gulf of California showing region of satellite image.

with in situ buoy data. After masking for land and clouds, 2 × 2 pixel arrays of the data were averaged to produce a smoothed SST image with a spatial resolution of approximately 2 km. Two examples of the final SST product are presented in Figures 2 and 3. The first image is from May 15, 1984, during one of the hydrographic cruises [*Bray*, 1988a].

The temperatures are coded in shades of gray with cooler temperatures being dark. (This coding is opposite to what is often seen in the literature and is done here to keep the images of the gulf from being too dark). Notice the region of cool SSTs around the midriff islands, with relatively warm SSTs over the shallow shelves in the north and to the

TABLE 1a. List of Satellite Images (March 1, 1984 to February 28, 1985)

Jday	Date	Sat	Proc	Clear
8406123	March 1, 1984	7	1	0.99
8406522	March 5, 1984	7	1	0.54*
8406923	March 9, 1984	7	1	0.99
8407322	March 13, 1984	7	1	0.22
8409323	April 2, 1984	7	1	0.79
8409423	April 3, 1984	7	1	0.99
8410123	April 10, 1984	7	1	0.94
8410223	April 11, 1984	7	1	0.99
8410322	April 12, 1984	7	1	0.93
8410422	April 13, 1984	7	1	0.94
8410923	April 18, 1984	7	1	0.97
8411122	April 20, 1984	7	1	0.98
8411723	April 26, 1984	7	1	0.49
8411823	April 27, 1984	7	1	0.97
8412822	May 7, 1984	7	1	1.00
8413323	May 12, 1984	7	1	0.79
8413622	May 15, 1984	7	1	0.97
8413722	May 16, 1984	7	1	0.54
8414223	May 21, 1984	7	1	0.99
8415023	May 29, 1984	7	1	1.00
8415123	May 30, 1984	7	2	0.83
8415823	June 6, 1984	7	1	0.86*
8416022	June 8, 1984	7	1	0.38
8416523	June 13, 1984	7	1	1.00
8416623	June 14, 1984	7	1	0.90
8416723	June 15, 1984	7	1	0.93
8417822	June 26, 1984	7	2	0.16
8418223	June 30, 1984	7	1	0.94
8419023	July 8, 1984	7	1	0.59
8419222	July 10, 1984	7	1	0.85
8419322	July 11, 1984	7	1	0.56*
8419422	July 12, 1984	7	1	0.12
8420023	July 18, 1984	7	1	0.47
8420922	July 27, 1984	7	1	0.53*
8421623	Aug. 3, 1984	7	1	1.00
8421722	Aug. 4, 1984	7	1	0.95
8422123	Aug. 8, 1984	7	1	0.43
8422223	Aug. 9, 1984	7	1	0.36
8422323	Aug. 10, 1984	7	1	0.56
8422423	Aug. 11, 1984	7	1	0.94
8422522	Aug. 12, 1984	7	1	0.52
8423322	Aug. 20, 1984	7	1	0.98
8424122	Aug. 28, 1984	7	1	0.95
8424222	Aug. 29, 1984	7	1	0.78
8424623	Sept. 2, 1984	7	1	0.82
8424723	Sept. 3, 1984	7	1	1.00
8424823	Sept. 4, 1984	7	1	0.97
8424922	Sept. 5, 1984	7	1	0.87
8425022	Sept. 6, 1984	7	1	0.77
8425423	Sept. 10, 1984	7	1	0.85
8425723	Sept. 13, 1984	7	1	1.00
8425822	Sept. 14, 1984	7	1	0.79
8426523	Sept. 21, 1984	7	1	0.78
8427123	Sept. 27, 1984	7	1	0.99
8427223	Sept. 28, 1984	7	1	0.97
8427422	Sept. 30, 1984	7	1	0.89
8427923	Oct. 5, 1984	7	1	0.75
8428222	Oct. 8, 1984	7	1	0.86
8428322	Oct. 9, 1984	7	1	0.47
8428923	Oct. 15, 1984	7	1	0.98
8429122	Oct. 17, 1984	7	1	0.65
8429623	Oct. 22, 1984	7	1	0.96
8429723	Oct. 23, 1984	7	1	0.80
8430022	Oct. 26, 1984	7	1	0.46
8430722	Nov. 2, 1984	7	1	1.00
8431023	Nov. 5, 1984	7	1	1.00
8431422	Nov. 9, 1984	7	1	0.99
8432322	Nov. 18, 1984	7	1	0.99
8432422	Nov. 19, 1984	7	1	0.74
8433122	Nov. 26, 1984	7	2	0.99
8433523	Nov. 30, 1984	7	1	1.00
8433823	Dec. 3, 1984	7	1	0.36

TABLE 1a. (continued)

Jday	Date	Sat	Proc	Clear
8433922	Dec. 4, 1984	7	1	0.76
8500123	Jan. 1, 1985	7	1	0.85
8500522	Jan. 5, 1985	7	1	0.87
8500922	Jan. 9, 1985	9	1	0.95
8501322	Jan. 13, 1985	7	1	0.34
8501723	Jan. 17, 1985	7	1	0.98
8501922	Jan. 19, 1985	9	1	0.99
8502021	Jan. 20, 1985	9	1	0.99
8503021	Jan. 30, 1985	9	1	0.53
8503921	Feb. 8, 1985	9	1	0.92
8504021	Feb. 9, 1985	9	1	0.68
8504722	Feb. 16, 1985	9	1	0.96
8504821	Feb. 17, 1985	9	1	0.79
8505121	Feb. 20, 1985	9	1	0.38
8505321	Feb. 22, 1985	9	1	0.75
8505821	Feb. 27, 1985	9	1	0.74

Jday, Julian day of satellite pass in UT (yydayhr); Sat, NOAA satellite number; Proc, processing session; Clear, fraction of oceanic data which is clear.

*Images not used in analysis because of location of clouds or inadequate cloud masking.

southeast of Tiburon Island. The second image is from November 9, 1984, during a second hydrographic cruise. During this period the northern shelf is cooler than waters directly offshore, and a cold plume of water is apparent near

TABLE 1b. List of Satellite Images (March 1, 1985 to February 28, 1986)

Jday	Date	Sat	Proc	Clear
8506320	March 4, 1985	9	1	0.38
8506821	March 9, 1985	9	1	0.20
8507221	March 13, 1985	9	1	0.12
8507821	March 19, 1985	9	1	0.98
8507921	March 20, 1985	9	1	0.98
8508021	March 21, 1985	9	1	0.44
8508121	March 22, 1985	9	1	0.31
8508721	March 28, 1985	9	1	0.46
8508821	March 29, 1985	9	1	0.94
8509422	April 4, 1985	9	2	0.40
8509521	April 5, 1985	9	1	0.90
8509621	April 6, 1985	9	1	0.96
8509721	April 7, 1985	9	1	0.97
8510422	April 14, 1985	9	1	1.00
8510621	April 16, 1985	9	2	0.72
8510721	April 17, 1985	9	1	0.70
8511322	April 23, 1985	9	1	0.85
8511421	April 24, 1985	9	2	0.62
8511621	April 26, 1985	9	2	0.66
8512322	May 3, 1985	9	2	0.80
8512521	May 5, 1985	9	2	0.40
8512621	May 6, 1985	9	2	0.34
8513321	May 13, 1985	9	2	1.00
8513421	May 14, 1985	9	2	0.89
8514222	May 22, 1985	9	2	0.98
8514321	May 23, 1985	9	2	0.91
8514421	May 24, 1985	9	2	0.92
8514521	May 25, 1985	9	2	0.41
8515221	June 1, 1985	9	2	1.00
8515421	June 3, 1985	9	2	0.58
8516221	June 11, 1985	9	2	0.71
8516321	June 12, 1985	9	2	0.75
8516421	June 13, 1985	9	2	0.14
8517221	June 21, 1985	9	2	0.83
8517321	June 22, 1985	9	2	0.43
8518022	June 29, 1985	9	2	0.85

TABLE 1b. (continued)

Jday	Date	Sat	Proc	Clear
8518121	June 30, 1985	9	2	1.00
8524622	Sept. 3, 1985	9	2	0.90
8524721	Sept. 4, 1985	9	2	0.98
8524821	Sept. 5, 1985	9	2	0.96
8525522	Sept. 12, 1985	9	2	0.42
8525621	Sept. 13, 1985	9	2	0.77
8525721	Sept. 14, 1985	9	2	0.90
8525821	Sept. 15, 1985	9	2	0.89
8526521	Sept. 22, 1985	9	2	0.99
8526621	Sept. 23, 1985	9	2	0.99
8526721	Sept. 24, 1985	9	2	0.81
8526821	Sept. 25, 1985	9	2	0.86
8526921	Sept. 26, 1985	9	2	0.11
8527422	Oct. 1, 1985	9	2	0.38
8527521	Oct. 2, 1985	9	2	0.71
8527721	Oct. 5, 1985	9	2	0.50
8527821	Oct. 6, 1985	9	2	0.37
8528421	Oct. 11, 1985	9	2	0.94
8528521	Oct. 12, 1985	9	2	0.99
8528621	Oct. 13, 1985	9	2	0.99
8528721	Oct. 14, 1985	9	2	0.78
8529322	Oct. 20, 1985	9	2	0.98
8529521	Oct. 22, 1985	9	2	0.96
8529621	Oct. 23, 1985	9	2	1.00
8529721	Oct. 24, 1985	9	2	1.00
8530321	Oct. 30, 1985	9	2	0.86
8530421	Oct. 31, 1985	9	2	0.98
8530521	Nov. 1, 1985	9	2	0.97
8530621	Nov. 2, 1985	9	2	1.00
8531222	Nov. 8, 1985	9	2	0.97
8531521	Nov. 11, 1985	9	2	0.74
8532122	Nov. 17, 1985	9	2	1.00
8532221	Nov. 18, 1985	9	2	0.95
8532521	Nov. 21, 1985	9	2	0.78
8533121	Nov. 27, 1985	9	2	0.78
8533321	Nov. 29, 1985	9	2	0.48
8533421	Nov. 30, 1985	9	2	0.79
8534022	Dec. 6, 1985	9	2	0.70
8534121	Dec. 7, 1985	9	2	0.70
8534221	Dec. 8, 1985	9	2	0.99
8535121	Dec. 17, 1985	9	2	1.00
8535221	Dec. 18, 1985	9	2	1.00
8535321	Dec. 19, 1985	9	2	1.00
8535922	Dec. 25, 1985	9	2	0.86
8536021	Dec. 26, 1985	9	2	0.81
8536121	Dec. 27, 1985	9	2	0.93
8536321	Dec. 29, 1985	9	2	0.93
8600322	Jan. 3, 1986	9	2	0.36
8600421	Jan. 4, 1986	9	2	1.00
8600521	Jan. 5, 1986	9	2	0.87
8600621	Jan. 6, 1986	9	2	1.00
8600721	Jan. 7, 1986	9	2	0.99
8601421	Jan. 14, 1986	9	2	0.76
8601521	Jan. 15, 1986	9	2	0.90
8601621	Jan. 16, 1986	9	2	0.99
8602222	Jan. 22, 1986	9	2	0.61
8602321	Jan. 23, 1986	9	2	0.92
8602421	Jan. 24, 1986	9	2	1.00
8602521	Jan. 25, 1986	9	2	1.00
8603221	Feb. 1, 1986	9	2	0.68
8603321	Feb. 2, 1986	9	2	0.96
8603421	Feb. 3, 1986	9	2	1.00
8603521	Feb. 4, 1986	9	2	0.75
8604122	Feb. 10, 1986	9	2	0.99
8604321	Feb. 12, 1986	9	2	0.68
8604421	Feb. 13, 1986	9	2	0.91
8605022	Feb. 19, 1986	9	2	0.69
8605221	Feb. 21, 1986	9	2	0.65
8605321	Feb. 22, 1986	9	2	0.82

Jday, Julian day of satellite pass in UT (yydayhr); Sat, NOAA satellite number; Proc, processing session; Clear, fraction of oceanic data which is clear.
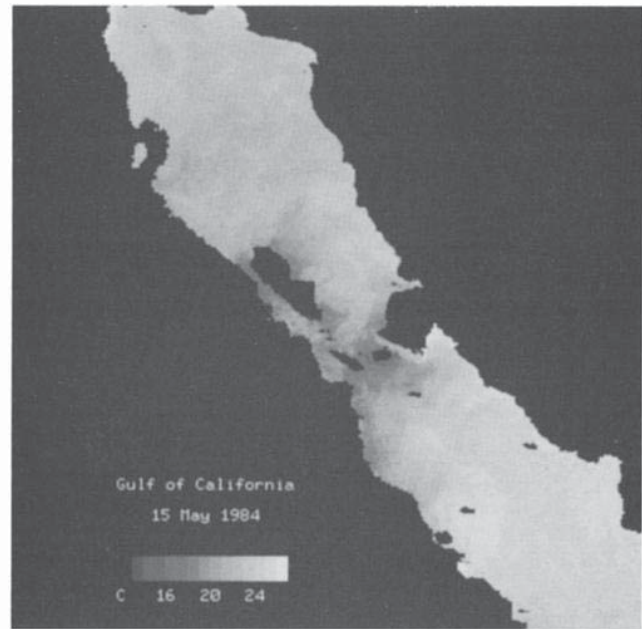

Fig. 2. AVHRR image of the sea surface temperature in the northern Gulf of California for May 15, 1984.

Tiburon Island. This cold plume appears to be the result of wind-induced upwelling which occurs predominantly during the fall and winter [Badan-Dangon et al., 1985].

To examine the seasonal variability, images were selected for the estimation of monthly mean SSTs (Figure 4). An effort was made to sample the spring-neap tidal cycle by using images that were separated by 6 to 10 days when possible. Images that were cloudy in the island region or over the shallow shelves were not used in the analysis, as SSTs in these regions were expected to have the largest response to tidal and atmospheric forcing. Significant surface heating in conjunction with an influx of moist, tropical

Fig. 3. AVHRR image of the sea surface temperature in the northern Gulf of California for November 9, 1984.
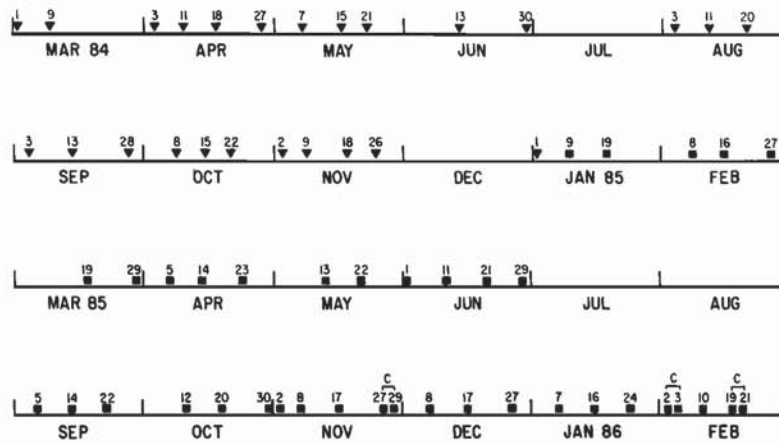
Fig. 4. Distribution of satellite data used to estimate monthly mean SST images for EOF analysis. Symbols denote NOAA 7 (inverted triangle) or NOAA 9 (square) afternoon pass. Numbers above symbols denote day of the month. ("C" denotes images that were composited).

air during the summer tended to obscure spatial temperature patterns during most of July and August in both years. In 1984 the December images were too cloudy to use. Most months had three to four clear images available for averaging. Composites of images separated by 1 or 2 days were made when large areas of data were missing. This was done only if significant gaps in the time series would otherwise occur.

In general, SST patterns within a particular month were fairly persistent, while the spatially averaged temperature fluctuated significantly. To avoid biasing estimates of the monthly mean SST in regions that contained clouds, the missing data were first replaced by the spatially averaged SST. This temperature was calculated by averaging over the remaining cloud-free pixels within each image. In this way any large-scale heating and cooling would be represented appropriately in the monthly means, and spatial patterns for the cloud-contaminated regions could be estimated from the remaining images in the month. The 20 resulting monthly mean images were used in an empirical orthogonal function (EOF) analysis of the SST variability in the northern Gulf of California.

4. EMPIRICAL ORTHOGONAL FUNCTIONS

The application of empirical orthogonal function analysis to satellite infrared data has previously been presented by *Kelly* [1985] and *Lagerloef and Bernstein* [1988]. EOFs are the principal axes of a data covariance matrix which, when ordered by eigenvalue, represent the dominant patterns of the variance. The data used to form the covariance matrix can then be represented as a linear combination of the eigenfunctions F_n,

$$T_s'(x, t) = \sum_{n=1}^{N} a_n(t)F_n(x) \tag{1}$$

with the coefficients or amplitudes a_n obtained by projecting the data onto each function,

$$a_n(t) = \sum_{x=1}^{M} T_s'(x, t)F_n(x) \tag{2}$$

where N represents the number of images used in the analysis and M is the number of spatial points in an image. By expressing the data in this way, most of the variability can be described by a few uncorrelated patterns whose temporal behavior can then be compared with that of other data fields [*Davis*, 1976].

Traditionally, EOFs are calculated for data in which the time-averaged mean at each location is removed prior to estimating the mean product matrix (which in this case is the data covariance matrix C):

$$T_s'(x, t) = T_s(x, t) - \frac{1}{N} \sum_{j=1}^{N} T_s(x, t_j) \tag{3}$$

$$C_{xy} = \frac{1}{N} \sum_{j=1}^{N} T_s'(x, t_j)T_s'(y, t_j) \tag{4}$$

Here, t_j signifies a particular image in the data set. The dominant eigenfunction or first mode (i.e., the function with the largest eigenvalue) will explain the largest portion of the temporal variability and is often associated with a seasonal signal in the data. Since all of the functions are orthogonal, the other patterns of variability will be perpendicular to the seasonal response of the system.

Recently, *Lagerloef and Bernstein* [1988] suggested that persistent features such as fronts or topographic eddies might be better described in an EOF analysis if the mean product matrix was formed from data in which the spatial average was first removed:

$$T_s'(x, t) = T_s(x, t) - \frac{1}{M} \sum_{x=1}^{M} T_s(x, t) \tag{5}$$

These eigenfunctions will be ranked according to the amount of spatial variability present in the data. That is, fairly persistent patterns with strong horizontal gradients will be described by the first mode, with subsequent modes being orthogonal. *Lagerloef and Bernstein* [1988] refer to these EOFs as "spatial EOFs" as compared to "temporal EOFs" when the time-averaged mean is removed from the data. For
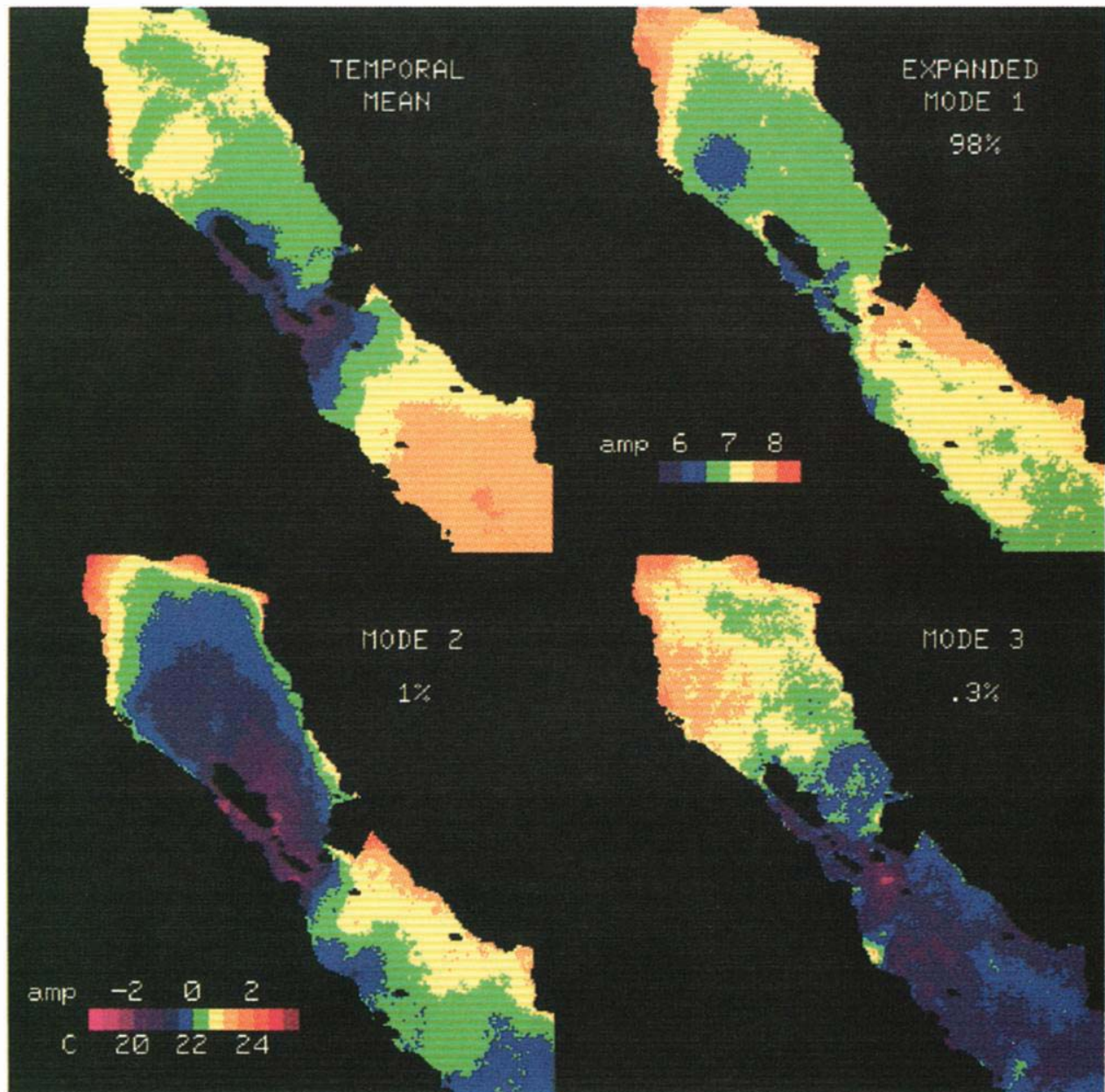
Plate 1.   Temporal mean and first three covariance EOFs. Mode 1 is shown with different scale than the other modes.

the purposes of discussion, EOFs calculated using data in which the spatial mean has been removed (equation (5)) will be referred to instead as "gradient EOFs," while those calculated using data in which the temporal mean has been removed (equation (3)) will be referred to as "covariance EOFs." This terminology will help avoid confusion between the two types of EOFs and the spatial amplitudes of the eigenfunctions versus the temporal amplitudes of the coefficient time series.

Although the calculation of the EOFs may be accomplished in a number of ways [*Kelly*, 1985, 1988; *Lagerloef and Bernstein*, 1988], the solution is unique provided there are no missing data. A singular value decomposition (SVD) of the data matrix, however, provides the most efficient way to calculate the EOFs [*Kelly*, 1988]. The analysis method is the same whether a time-averaged mean or spatially averaged mean is removed from the data (or both), but the

resulting EOFs are different because a different mean product matrix is generated in each case. The satellite images used in forming the mean product matrix can be reconstructed using any one of these sets of EOFs plus the corresponding mean field that was initially removed.

Both the covariance and gradient EOF analyses are presented below. Each gives a different perspective of the SST variability and permits one to form a more complete interpretation of the processes important in producing those patterns.

4.1.   Covariance EOFs

Empirical orthogonal functions of the SST covariance were calculated using the 20 monthly mean images. The temporal mean and first three modes of the EOF analysis are presented in Plate 1. The mean field shows a cold pool of
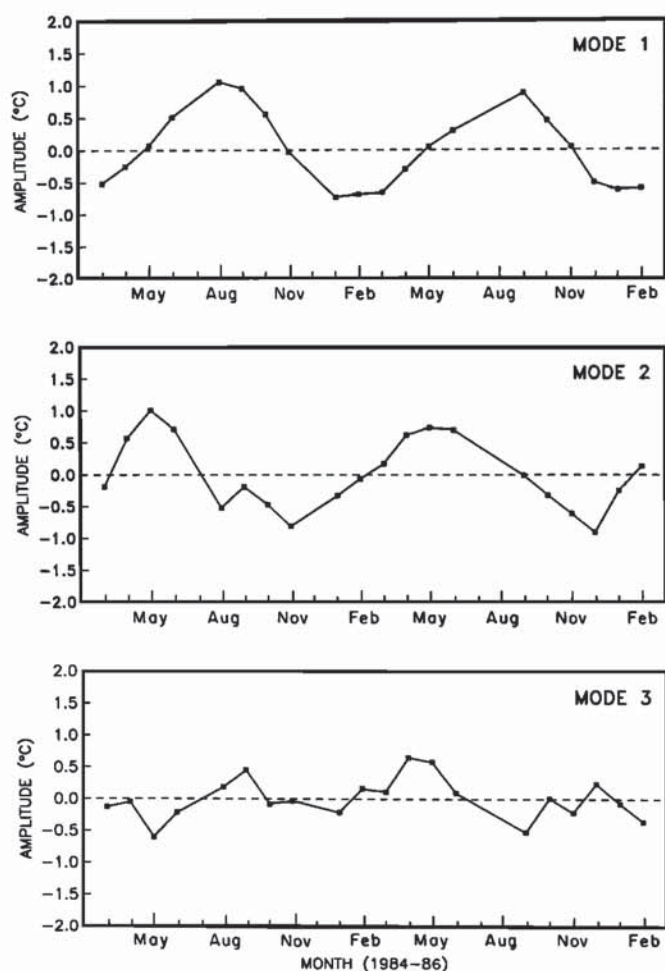
Fig. 5. Amplitude time series for the covariance EOFs.

water in the island region. This feature was previously noted by *Badan-Dangon et al.* [1985] in earlier studies of satellite infrared imagery of the Gulf of California. Here, however, isolated temperature minima can be seen in the Ballenas, Salsipuedes, and San Esteban channels, with the coldest temperatures near San Esteban Island. To the north, warmer temperatures are associated with the shallow shelf as well as the Delphin Basin. South of the islands, temperatures increase with distance from the island region, with the largest SSTs occurring in the southern Guaymas Basin. A strong SST gradient exists between the island region and the Guaymas Basin, with a wedge of cold water extending south along the Baja California coast. A similar front is not seen north of the islands.

The first mode explains 98% of the sea surface temperature variability (Plate 1). The spatial amplitudes are all positive, with larger values over the shallow shelves in the north and to the southeast of Tiburon Island. Small spatial amplitudes are present in the Delphin Basin and near the island of Angel de la Guarda with moderate amplitudes present over most of the Guaymas Basin. This mode describes patterns associated with the dominant seasonal cycle of the sea surface temperature. The mode 1 temporal amplitudes (Figure 5) show maximum surface temperatures for the northern gulf occurring in August, with minimum SSTs in January. An EOF analysis of historical hydrographic sec-

tions from the Guaymas Basin [*Bray*, 1988*a*] showed maximum mode 1 water column temperatures occurring in August as well; however, the coldest temperatures occurred in March. Subinertial temperatures measured at 10 m on the Guaymas and Santa Rosalia shelves during 1984 [*Merrifield and Winant*, 1989] had seasonal cycles similar to those observed in the hydrographic data. Since the surface mixed layer is deeper in the winter than in the summer, the mismatch in the timing of the winter minimum is not likely to be due to measuring the surface skin temperature versus the temperature at depth. The discrepancy in the seasonal behavior of the mode 1 SSTs and the in situ temperatures most likely occurs because EOFs by definition describe patterns that covary. If the Guaymas Basin is forced somewhat differently than the rest of the northern gulf, then mode 1 will describe only that portion of the SST variability which is correlated with the variability in the island region and northern basin.

When the mode 1 temporal amplitudes are positive during June through October, warm temperatures on the northern shelf surround a cool SST anomaly in the Delphin Basin. From November through April the pattern is reversed, with shelf temperatures being colder than offshore. *Bray* [1988*a*] estimated baroclinic velocities for two hydrographic sections across the Gulf of California: one in the Guaymas Basin from Guaymas to Santa Rosalia, and the other in the northern basin across a section just south of a line connecting Puerto Peñasco and San Felipe. For both of these sections the surface currents were cyclonic during the summer and anticyclonic during the rest of the year, with stronger currents in the summer (Figure 6). The mean currents on the Santa Rosalia and Guaymas shelves also showed a seasonally reversing circulation pattern [*Merrifield and Winant*, 1989]. SST patterns in the northern basin are consistent with the circulation inferred from the hydrography. The minimum in the EOF spatial amplitudes in the Delphin Basin corresponds approximately to the center of the gyre [*Bray*, 1988*b*], and the larger mode 1 amplitudes during the summer are consistent with the increased geostrophic current velocities.

The mode 1 spatial amplitudes in the Guaymas Basin are generally larger in the east, with a narrow band of smaller amplitudes along the Baja California peninsula. This pattern suggests that SSTs on the eastern side of the gulf have a more pronounced seasonal signal than SSTs along the Baja California peninsula. Near-surface temperatures (10 m) measured on each shelf in the Guaymas Basin also show a larger seasonal signal on the eastern side, with maximum temperatures in August and minimum temperatures in March similar to the hydrographic measurements [*Merrifield and Winant*, 1989]. This behavior is attributed to seasonal patterns of coastal upwelling. During the summer, relatively weak winds blowing from the southeast are upwelling favorable for the Baja coast. Introduction of cooler upwelled water would moderate the warm summer temperatures on the western side, while stronger northwesterly winds would produce colder temperatures on the opposite shelf during the rest of the year. This modulation of the seasonal temperatures could explain the enhanced seasonal signal observed on the eastern side of the Guaymas Basin. However, cold plumes of water observed along the Baja California coast [*Badan-Dangon et al.*, 1985] could also be caused by the advection of tidally mixed waters from the island region. The introduction of this colder water into the large-scale cyclonic
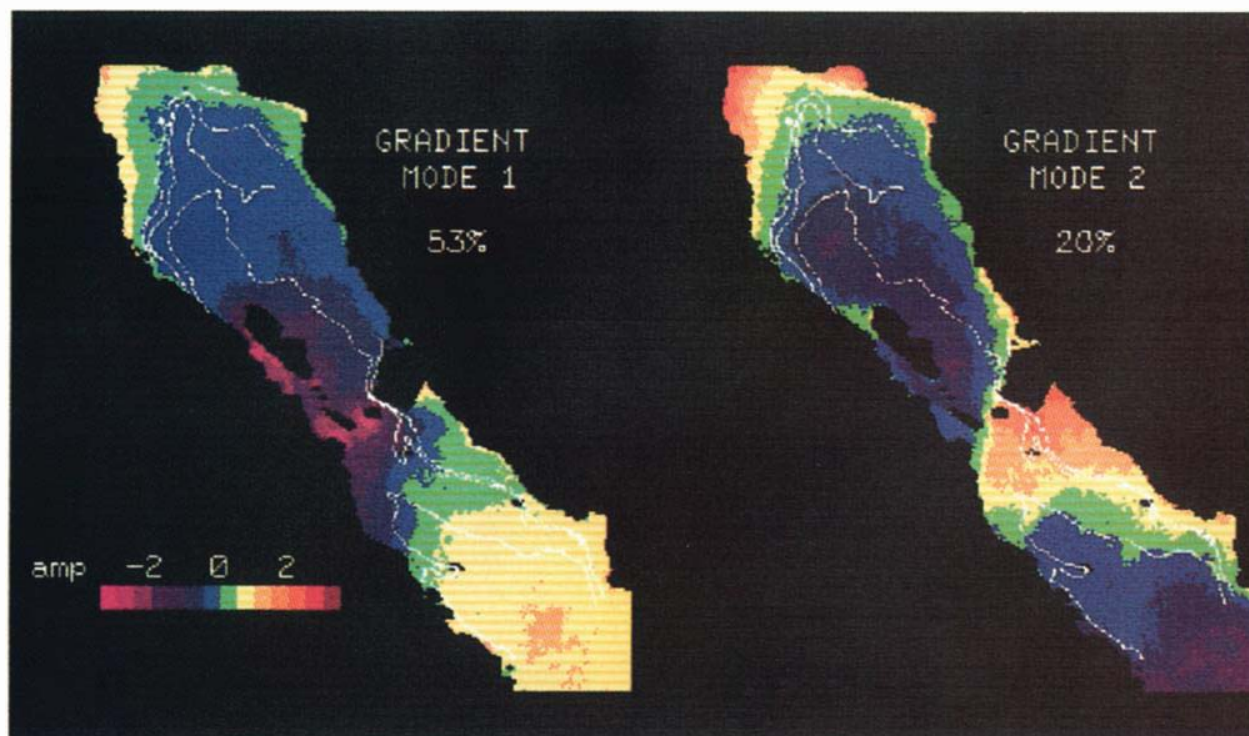
Plate 2. Gradient EOF modes 1 and 2 with bathymetry.

circulation could produce SST patterns resembling upwelling plumes and could also explain the difference in SST variability between the two coasts.

Mode 2 represents 1.1% of the total SST variance (43% of the nonseasonal variance) and distinguishes the behavior of the shallow shelf regions relative to the rest of the gulf (Plate 1). Strong gradients in the spatial amplitudes can be seen on the northern shelf, with a change in sign occurring near the shelf slope (see Figure 1). The contours of the mode appear to coincide with the bathymetry in the northern basin, with maximum positive amplitudes occurring in the shallowest regions of the Colorado River delta. Large negative amplitudes occur near the islands with minima in the Ballenas Channel and along the coast near Salsipuedes Sill. Positive amplitudes are present along most of the eastern side of the gulf, especially to the southeast of Tiburon Island, indicating that temperatures there covary with temperatures on the northern shelf. The temporal amplitudes show that the shelf temperatures are significantly warmer than offshore during late spring and early summer and colder during the winter (Figure 5).

Mode 3 (Plate 1) represents 0.3% of the total variability (14% of the nonseasonal variance), with the northern basin and island region out of phase with the Guaymas Basin. The behavior of the temporal amplitudes (Figure 5) does not repeat in the second year of data, suggesting that this mode is not related to seasonal variations in the forcing fields as observed for modes 1 and 2.

4.2. Gradient EOFs

To examine the large-scale SST gradients in the Gulf of California, the spatially averaged SST was subtracted from each monthly mean image before calculating the EOFs. The spatial mean SSTs exhibit a seasonal cycle (Figure 7) with a maximum in August of 30.5°C and a minimum in January of approximately 17°C. These temperatures, however, do not reflect the absolute temperature extremes in the gulf, which range from below 14°C in January to over 32°C in late August and early September.

The first two gradient EOFs are presented in Plate 2 along with selected bathymetric contours (60, 80, 100, 200, and 1000 m; see Figure 1). Mode 1 explains 53% of the SST variance and has positive amplitudes over the shallow shelf region in the northern basin and throughout the Guaymas Basin, with relatively large negative amplitudes associated with the channels and sills in the island region. Gradient mode 1 is similar in pattern to the temporal mean and distinguishes the behavior of the cold pool of water around the island region. The zero crossing for the mode corresponds approximately to the 80-m isobath over the shelf slope in the north and to the head of the Guaymas Basin south of the islands. The steepening of the slope and narrowing of the shelf along either coast in the north is also evident in the EOF pattern, suggesting that the SST variability described by this mode is related to the bathymetry. Although the resolution of the graphics does not permit contouring of the channel region, comparison of the negative anomalies with the map in Figure 1 shows that their positions correspond to the location of relatively shallow regions associated with the islands and channels. Note the large negative values associated with the narrowing of Ballenas Channel near the island of Angel de la Guarda, as well as those over Salsipuedes and San Esteban sills and along the shallow region connecting Angel de la Guarda with the island to the south. No negative anomaly, however, can be distin-
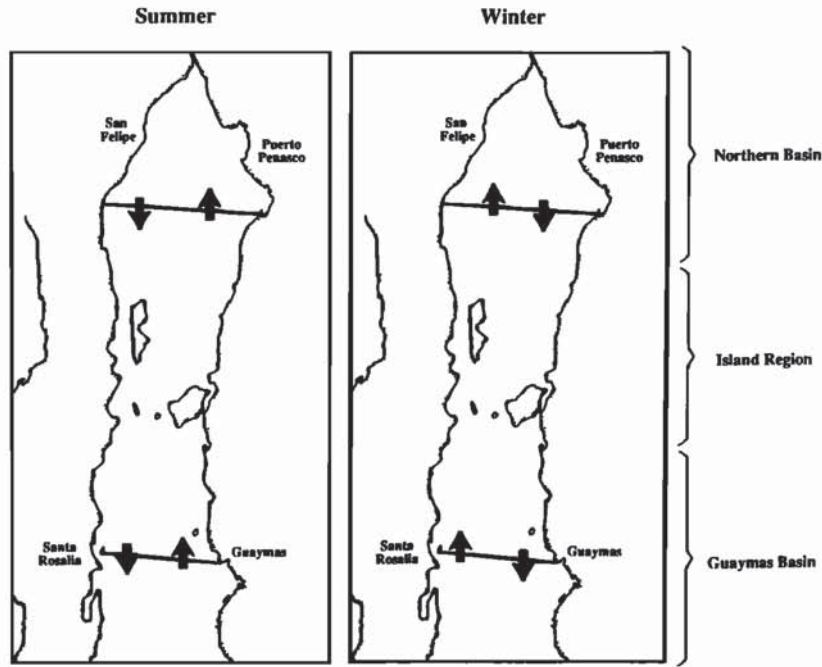
Fig. 6. Schematic of the summer and winter circulation in the Gulf of California as estimated from hydrographic observations of the upper ocean [*Bray*, 1988*a*].

guished in Tiburon Channel between San Estaban Island and Tiburon Island.

The temporal amplitudes of the gradient EOF functions are presented in Figure 8. The mode 1 amplitudes are positive with a bimodal shape. The first maximum occurs in May, with a smaller second maximum in September. Since the variability described by this mode is correlated with the bathymetry and contains SST features believed to be related to tidal mixing, we compared the temporal behavior of this mode with the variability in the tidal range. The tidal range used in the comparison is the maximum daily difference between high and low water for the predicted tides at Puerto

Peñasco [*Universidad Nacional Autónoma de México*, 1969]. Since the whole northern basin has approximately the same tidal phase [*Filloux*, 1973], the tidal range at Puerto Peñasco can be used to parameterize the variability in the volume of water exchanged through the channels in the island region and thus the magnitude of the currents. The maximum and average tidal range for each month are plotted in Figure 9 along with the gradient mode 1 temporal amplitudes. The same bimodal behavior seen in the temporal amplitudes is also evident in the seasonal behavior of the tides. The largest monthly mean tidal ranges occur in April–May and July–August, somewhat earlier than the mode 1
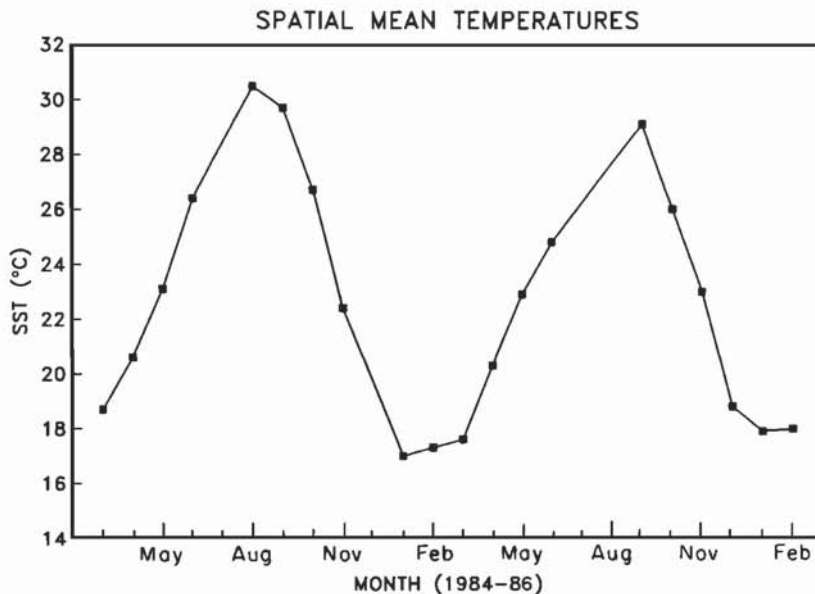
Fig. 7. Time series of spatially averaged sea surface temperatures for monthly mean images.

amplitude maxima, with the primary minima occurring in December in both cases.

The bimodal behavior of the gradient mode 1 amplitudes can be rationalized in terms of the seasonal variability in the stratification of the water column and spatial patterns of tidal mixing. In the spring, when SSTs are increasing but the stratification is still weak, tidal mixing will create large temperature differences between the island region and the rest of the gulf. These gradients are established because tidal mixing in the island region occurs over much greater depths than are possible over the shallow northern shelf. Thus in the presence of a uniform positive heat flux, temperatures on the shallow shelf will be warmer because the heat is distributed over a smaller volume of water than in the island region. As summer progresses, increased stratification [*Bray*, 1988a] suppresses tidal mixing throughout the gulf, minimizing these temperature gradients. In the fall, increased tidal currents in conjunction with seasonal cooling break down the stratification, reestablishing temperature differences between the island region and elsewhere. These gradients are again reduced when convective cooling in combination with small tidal ranges results in fairly uniform temperatures. The smaller temporal amplitude in the fall may be due to the fact that strong gradients are not able to form before seasonal cooling begins to eliminate them.

Gradient mode 2 (Plate 2) explains 20% of the spatial variability and, like mode 2 in the covariance analysis, has

Fig. 9. Comparison of the amplitude time series for gradient mode 1 with the average and maximum monthly tidal range at Puerto Peñasco.

Fig. 8. Amplitude time series for the gradient EOFs.

large positive amplitudes on the shallow northern shelf as well as on the broad shelf to the southeast of Tiburon Island. This mode, however, shows an extension of the positive amplitudes across the gulf at the head of the Guaymas Basin similar to upwelling patterns observed in the image from November 9, 1984 (Figure 3). The zero crossing of the mode in the Guaymas Basin corresponds approximately to the 1000-m isobath. On the northern shelf the largest amplitudes occur in the shallowest portions of the Colorado River delta and in the Adair and San Jorge bays just north of Puerto Peñasco. In these shallow embayments, significant gradients in the spatial amplitudes occur just inshore of the 60-m isobath (see Figure 1) where tidal mixing fronts have been observed and predicted to occur [*Argote et al.*, 1985] by the h/u^3 criterion of *Simpson and Hunter* [1974]. Note the three closely spaced isolines of variability which may be related to seasonal changes in the position of a tidal mixing front. The zero crossing of mode 2 is also associated with the shelf slope in the northern basin though not as closely as in mode 1.

Gradient mode 2 temporal amplitudes (Figure 8) have a sinusoidal behavior with maximum positive amplitudes in June and maximum negative amplitudes in November–December. The seasonal along-gulf winds at Tortuga Island in the Guaymas Basin (Figure 10) demonstrate a similar sinusoidal behavior with maximum northward winds from June through August and maximum southward winds from November through February. The along-gulf winds are fairly
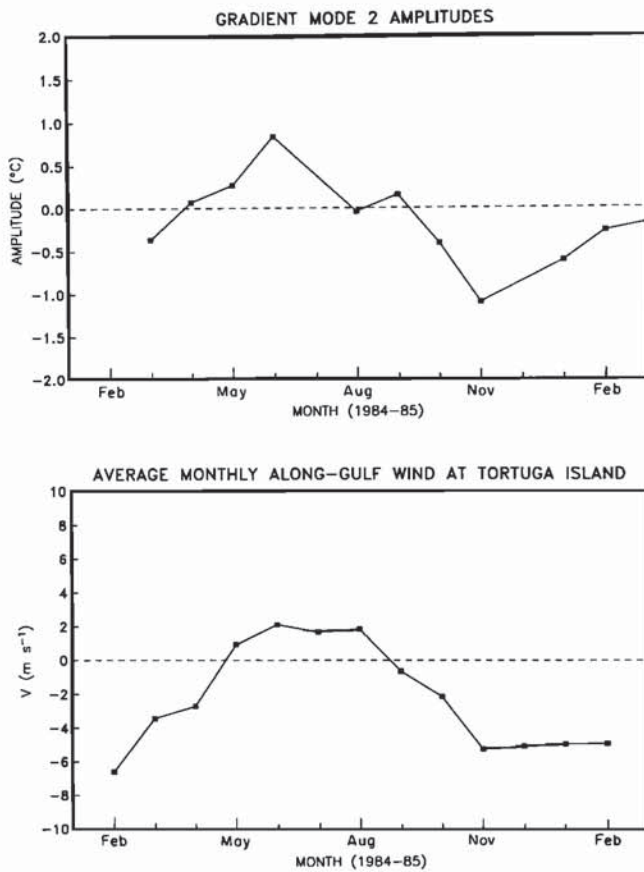
Fig. 10. Comparison of the amplitude time series for gradient mode 2 with the monthly averaged winds at Tortuga Island.

coherent over most of the gulf, with winds at Tortuga Island being most representative of the large-scale wind field [*Merrifield and Winant*, 1989]. The discrepancy between the wintertime minima in the two time series probably results from the decreased surface signature of upwelling during the later winter months. Although the wind is still blowing strongly from the northwest, SSTs of the upwelled water will be more similar to surrounding SSTs during the winter than during late fall, thus reducing the contribution of the shelf mode to the overall SST variability. Temperatures on the shallow northern shelf are covarying with those generated by upwelling off Tiburon Island. The cooler temperatures in the north most likely result from local differences in the surface heat flux. When the seasonal winds reverse in the fall, cool, dry air from over the continental United States blows southeastward across the northern basin [*Badan-Dangon et al.*, 1991]. The northern shelf would be most subject to cooling, since the air mass is colder and lower in water vapor content when first coming off the continent. This differential heating and cooling of the northern shelf was also observed in heat flux calculations made by *Lavin and Organista* [1988].

Gradient mode 3 (not shown) explains 7% of the spatial variability. It is essentially identical to mode 3 of the covariance analysis (Plate 1) with the northern basin and island region out of phase with the rest of the gulf. The spatial pattern resembles patterns observed in the gulf during spring and summer when warm SST anomalies are often present in the northern basin and island region. To the eye,

these features resemble low-lying clouds with temperatures comparable to those found further south in the gulf. Similar features were also observed by *Badan-Dangon et al.* [1985] in an analysis of satellite infrared images from the spring and summer of 1980. They hypothesized that the warm SST patches resulted from spatial variations in the intense heat and moisture fluxes. These features will be analyzed further when shorter time scales are examined below.

Separate gradient EOF analyses were performed for each year of satellite data (March 1984 to February 1985 and March 1985 to February 1986). Both years showed SST patterns similar to those described above. This suggests that the SST patterns are repeatable from year to year and very likely reflect the seasonal forcing of the upper ocean.

5. SHORT-TERM VARIABILITY

Empirical orthogonal functions do not necessarily reflect variability in the data that can be attributed to one particular forcing mechanism. If the patterns of SST variability observed in the gradient EOF analysis are indeed the result of tidal and atmospheric forcing of the upper ocean, the behavior of these modes on shorter time scales might be expected to resemble the variability in the surface heat flux, tides, and winds. To check this, the spatially averaged SST and the temporal amplitudes for the first two gradient EOFs were estimated for 71 images which were at least 50% cloud-free (see Table 1a). These images spanned the period March 1984 through February 1985, when wind and meteorological data were also collected in the gulf as part of the field experiment (Figure 11). When no data are missing from the individual satellite images, the temporal amplitudes are obtained from the inner product of the demeaned images and the corresponding eigenfunctions,

$$a_n(t_j) = \sum_{x=1}^{M} T'_s(x, t_j) F_n(x) \qquad (6)$$

where M is the total number of ocean pixels in an image. Since clouds are almost always present to some degree, the amplitudes and spatial mean SST for each image must be estimated. We want to find those temporal amplitudes which, when multiplied by their corresponding modes, will estimate the SST field with the minimum amount of error in the least squares sense. This is done by solving the overdetermined system of equations

$$T_s(z, t_j) = b_0(t_j)\hat{G}_0(z) + \sum_{n=1}^{N'} b_n(t_j)\hat{G}_n(z) \qquad (7)$$

for each image or time, t_j [*Kelly*, 1985]. The values $\hat{G}_n(z)$ are those values of the gradient eigenfunctions $G_n(x)$ which correspond to the available clear ocean data $T_s(z, t_j)$ in an image. Since we are also estimating the spatial mean temperature (b_0), a vector of ones ($\hat{G}_0$) is included in the analysis. This system consists of a set of M' equations in ($N' + 1$) unknowns, where M' is the number of available clear ocean pixels in a given image (>9000 for this analysis) and N' is the number of mode amplitudes to be estimated (two in this case). An equivalent system of equations is solved for each image to obtain a time series of estimated amplitudes for each of the EOFs. The estimated spatially
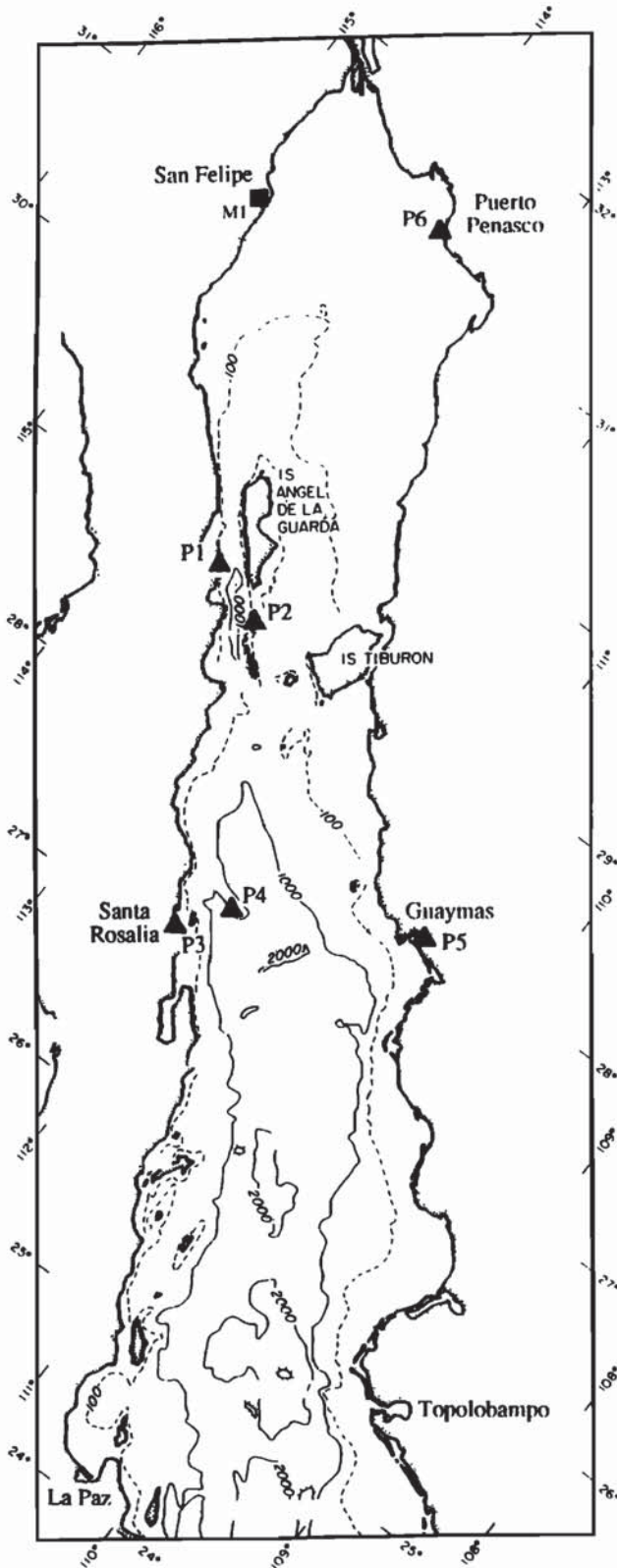
Fig. 11. Map of the Gulf of California showing locations of the PAM (triangles) and Mexican Meteorological Service (square) weather stations: Isla Piojo (P1), Isla Raza (P2), Santa Rosalia (P3), Isla Tortuga (P4), Guaymas (P5) Puerto Peñasco (P6), and San Felipe (M1).
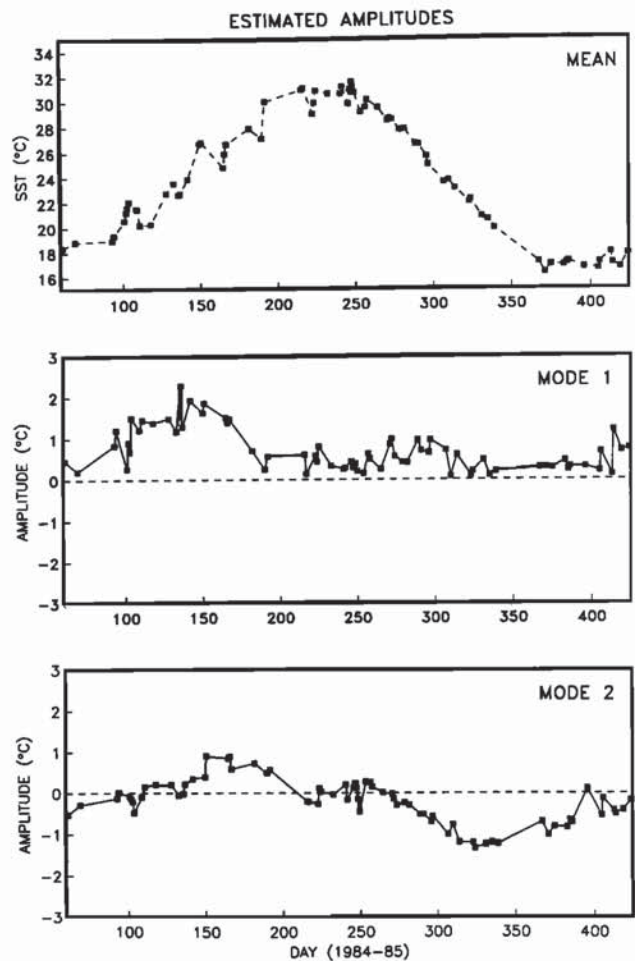

Fig. 12. Estimated spatial mean and gradient mode 1 and 2 amplitudes for 71 images spanning the period March 1, 1984, through February 28, 1985. Days are numbered consecutively from January 1, 1984.

averaged SST and the amplitudes of the first two gradient EOFs are presented in Figure 12. In the following sections the temporal behaviors of these amplitudes are compared to the variability observed in the forcing fields.

5.1. Surface Heating

The estimated spatial mean temperatures of the individual images reveal a seasonal cycle with additional short-term variability during the spring and summer (Figure 12). This variability is also seen regionally, with spatially averaged SSTs in the northern basin, island region, and Guaymas Basin varying similarly (Figure 13). Daily variations in the spatially-averaged temperature were also observed by *Kelly and Davis* [1986] in SSTs off the northern coast of California obtained from NOAA 6 infrared data. The observed fluctuations were attributed to changes in the satellite-target view angle which determines the amount of atmosphere through which the sea surface is observed. Absorption of the up-welled radiation by water vapor in the atmosphere reduces the amount of radiation that would otherwise reach the satellite sensor, resulting in the measurement of a SST that appears cooler than it actually is. The wider the view angle, the larger the amount of water vapor between the sea surface
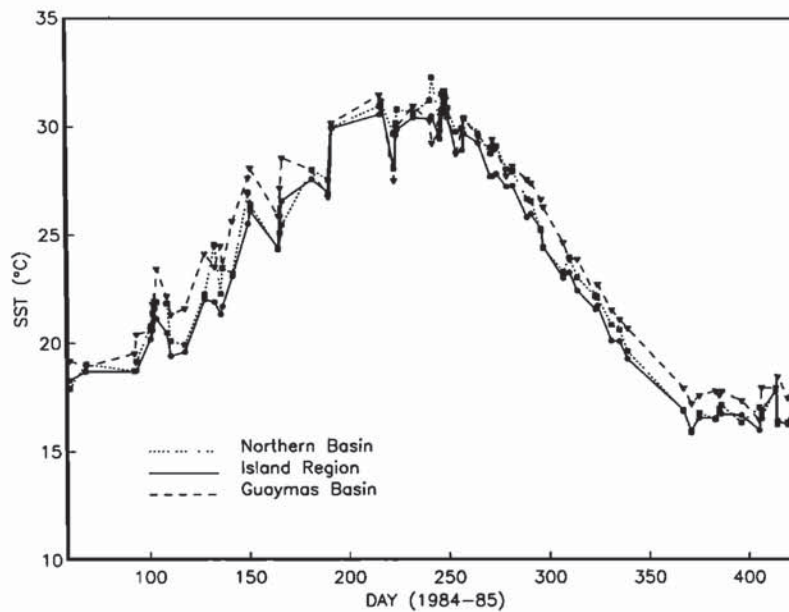
Fig. 13. Time series of spatially averaged SSTs for the northern basin, island region, and Guaymas Basin showing correlation in temperature fluctuations. Days are numbered consecutively from January 1, 1984.

target and the satellite and the larger the error in the SST calculation. A correction for this effect depends on the use of two infrared channels that contain wavelengths that are sensitive primarily to changes in the water vapor concentration. On the NOAA 6 satellite, however, one of the two available infrared channels was also sensitive to reflected sunlight. With the inclusion of a third infrared channel on subsequent satellites, the problems associated with atmospheric water vapor were expected to be corrected. A comparison of the cosine of the satellite-target view angle (cos θ) and the detrended spatial mean temperatures for the Gulf of California (Figures 14a and 14b) shows that for the NOAA 7 and NOAA 9 satellite data the two time series are uncorrelated ($r = 0$). The MCSST algorithms appear to be fairly successful in correcting for atmospheric water vapor in these data, so that variations in the satellite-target view angle would not explain the 2°–3° changes observed in the SST over several days.

Another possible cause for the large fluctuations in the spatially averaged SST is variability in the heating of the surface layer. Note that the fluctuations occur only in the spring and summer, when the sea surface is warming. During the fall and winter the SST decreases fairly smoothly until February, when the fluctuations are seen again as the ocean begins to warm. Air temperatures for each region of the gulf are plotted in Figure 15 along with the spatially averaged SST for each of the 71 images (denoted by boxes, both open and solid). Note the strong correlation between the two time series during the spring and summer, when large, short-period changes in air temperature are accompanied by corresponding changes in the sea surface temperature. The large fluctuations in air temperature appear to be associated with synoptic weather events which produce pulses of cold, dry air from the north [Badan-Dangon et al., 1991]. Because the ocean and atmosphere attain heat and moisture equilibrium fairly quickly, a high degree of correlation is observed. Air temperatures during the fall and winter, however, are colder and much more variable than the SSTs. During this time of year, convective

cooling and larger wind stresses would produce a deeper surface mixed layer. SST fluctuations are thus minimized because changes in heat content are occurring over a larger volume of water than when the surface is stratified.
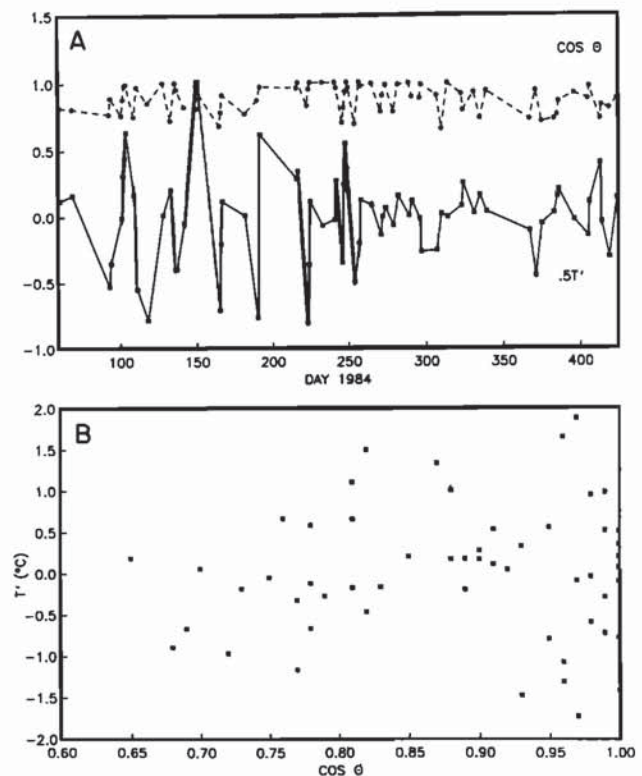

Fig. 14. (a) Comparison of the variability in the spatially averaged SST (detrended and scaled for plotting) and the cosine of the satellite-target view angle. Days are numbered consecutively from January 1, 1984. (b) Scatter plot of the same two data sets shown above.
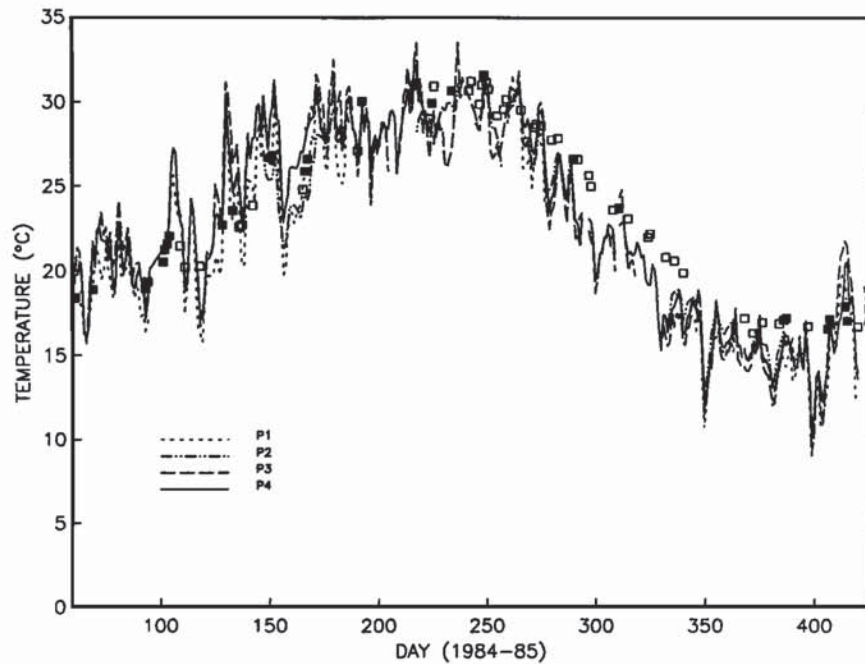
Fig. 15. Spatially averaged SSTs of the satellite images (open and solid boxes) plotted along with the daily averaged air temperature at selected meteorological stations: Isla Piojo (P1), Isla Raza (P2), Santa Rosalia (P3), and Isla Tortuga (P4). Solid boxes denote images that contain warm SST anomalies. Days are numbered consecutively from January 1, 1984.

During the spring and summer, relatively warm SST anomalies can also be seen in the satellite images (solid boxes in Figure 15 refer to images which contain the warm anomalies). These features occur primarily north of the islands and resemble low-lying clouds or fog in the satellite images (Figure 16). The temperatures, although warmer than the surrounding sea surface, do not lie outside the range of temperatures expected in the Gulf of California. Note the warm patches north of Tiburon Island and near San Felipe in the northern basin. Such features are usually associated with smaller-scale SST anomalies which can be seen upon careful inspection of Figure 16 (the dark spots in the northern basin are masked clouds). Similar anomalies were observed in the northern gulf during spring and summer 1980 [*Badan-Dangon et al.*, 1985]. Although a specific cause could not be determined, it was thought that these anomalies were associated with spatial variability in the air-sea interaction over the northern basin. In the present analysis it is apparent that these SST anomalies occur primarily during warming events in the gulf (Figure 15). In a series of four images from April 1984 (Julian days 101–104), for example, a dramatic increase in the areal extent of these warm surface anomalies occurs in the northern gulf as the air temperature rises. Similar anomalies do not generally occur in the fall or winter nor during local cooling events in the spring and summer.

During March 1984, a Barnes PRT-5 radiometer was flown aboard a National Center for Atmospheric Research (NCAR) aircraft at an altitude of approximately 30 m. These observations were made as part of a study of the lower atmosphere over the Gulf of California [*Candela et al.*, 1985]. One of the overflights corresponds with the image presented in Figure 16, and the portion of the flight path containing retrievable radiometer data is superimposed on the satellite image. A comparison of 10 km by 10 km averages of the two data sets is presented in Figure 17. The data bins correspond to the sequential 10 km by 10 km sections of data along the flight path beginning at the northern end of the gulf. The center of each data bin is denoted by a white dot in Figure 16 which combined mark the flight path of the aircraft. Note that the satellite-derived

Fig. 16. AVHRR image for March 9, 1984, showing warm sea surface temperature anomalies in the northern gulf. The locations of the NCAR radiometer measurements are indicated by the flight path.
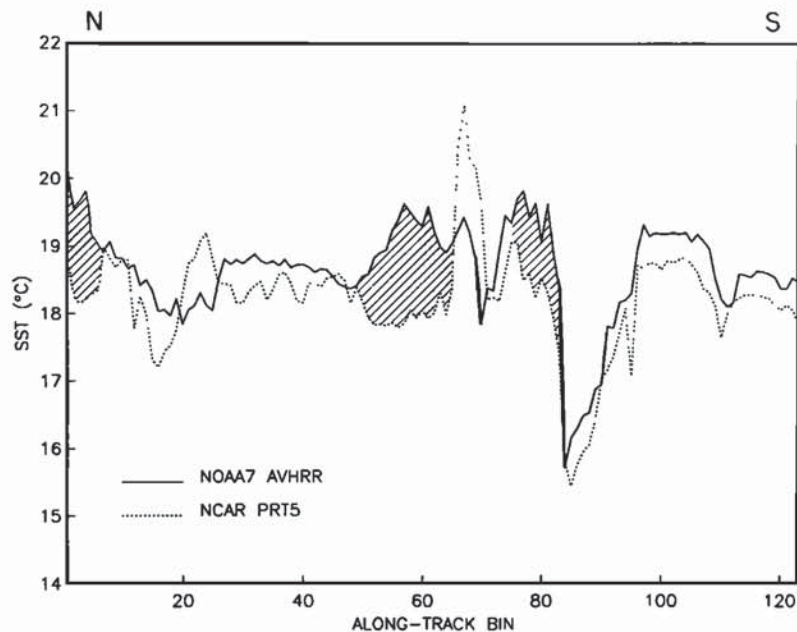
Fig. 17. Comparison of the AVHRR-derived SST and the SST measured 30 m above the surface by a Barnes PRT-5 radiometer flown aboard an NCAR plane. Data were measured along the north-south path indicated in Figure 16. Hatched areas correspond to warm anomalies visible in satellite image. The large warm peak in the NCAR data corresponds to flight over land at southern end of Isla Angel de la Guarda.

temperatures of the anomalies are approximately 2°C warmer than the near-surface SST measurements (the large spike in the NCAR temperatures is due to the plane flying over land). The temperature difference is somewhat enhanced because of the time difference in the two measurements. The aircraft overflight occurred in the morning, several hours prior to the satellite pass, as is apparent by the consistently warmer satellite temperatures. The relatively large difference between the two measurements in the anomalously warm regions could be the result of water vapor in the lower atmosphere. However, a lack of similar features in the Guaymas Basin, where spatially averaged SSTs covary with those of the island region and northern basin (Figure 13), suggests that the increase in the satellite-derived SSTs during warming events is related to an actual increase in the temperature of the sea surface. Since the satellite pass occurs several hours after the aircraft overflight, it is more likely that these anomalies represent regions of intense warming during the late afternoon. This would occur if the winds are generally weak but spatially variable. In that case, regions of consistently low wind speed would be much warmer. Wind speeds on the day of the image were 2 m/s or less over most of the northern gulf, with particularly weak winds in the regions where the warm SST anomalies are observed [Candela et al., 1985].

5.2. Tidal Mixing

The estimated amplitudes for gradient mode 1 (Figure 12) exhibit significant short-term variability in addition to the same general behavior observed in the amplitude time series for the monthly mean images (Figure 8). To check whether the SST patterns revealed in gradient mode 1 do result from tidal mixing, the behavior of the estimated amplitudes is compared to the variability in the daily maximum tidal range at Puerto Peñasco. Because of the additional spatial variabil-

ity introduced by the presence of the warm SST anomalies during the spring and summer, the analysis will be restricted to a series of 27 images which span approximately 100 days from the end of August to the beginning of December 1984 (Julian days 240 to 340). The detrended amplitudes for gradient mode 1 are plotted in Figure 18, along with the detrended maximum daily tidal range for Puerto Peñasco. These two time series are significantly correlated ($r = 0.56$) at a lag of 4 days, with the tidal range leading the mode 1 amplitudes. The maximum correlation between the tidal range and the mode 1 SST pattern occurs approximately halfway between spring and neap tides. This means that the strongest temperature gradients during the fall and early winter are occurring several days after the largest tidal ranges. The SST patterns observed may in fact be generated when cold SSTs are mixed horizontally, rather than being generated locally by spatially varying tidal mixing. This would account for the lagged correlation, which would now be dependent on time scales of horizontal eddy diffusivity and restratification of the water column. Since the images during the fall appear to resolve a fortnightly modulation of the SST, we should be able to determine where tidal mixing is the strongest by estimating the SST response to the tidal forcing using a linear statistical model.

Linear statistical model. A linear statistical model can be used to examine the ocean response to a particular forcing field [Davis, 1976]. Ideally, the response coefficients are estimated from a long time series of data; however, satellite data are inherently gappy owing to cloud cover and the precession of the satellite orbit. This makes it difficult to model short-time-scale variability with any accuracy. As we saw in the previous section, the estimated amplitudes for 27 images in the fall of 1984 varied with the spring-neap tidal cycle, indicating that the SST fluctuations associated with the tidal forcing may be recoverable. By carefully selecting
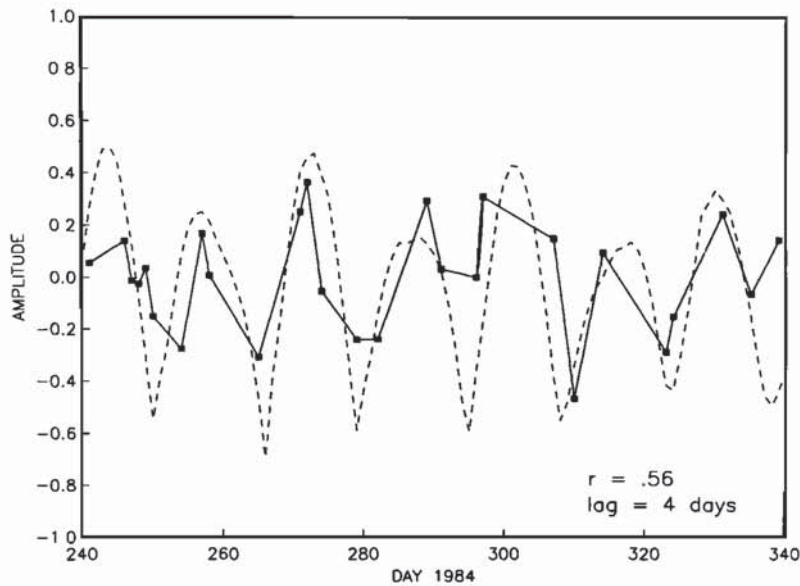
Fig. 18. Comparison of the detrended gradient mode 1 amplitudes for individual images between August 28, 1984, and December 4, 1984 (solid line) and the maximum daily tidal range at Puerto Peñasco (rescaled for plotting). Maximum correlation ($r = 0.56$) occurs at a lag of 4 days, with the largest SST gradients occurring approximately 4 days after the largest tidal ranges.

images that are fairly cloud-free and that sample the data primarily at spring and neap tides when the largest changes in SST occur, we may be able to estimate the tidal response of the SST in the Gulf of California. Of the 27 images available in the fall, 13 satisfied these criteria (Figure 19). These 13 images are used to estimate the spatially varying response coefficients, $\alpha(x)$, for the linear statistical model:

$$T_s'(x, t_j) = \alpha(x)h(t_j) \qquad (8)$$

where $h(t_j)$ is the maximum tidal range (m) at Puerto Peñasco for the day of the image and

$$\alpha(x) = \frac{\langle T_s'(x, t_j)h(t_j)\rangle}{\langle h(t_j)h(t_j)\rangle} \qquad (9)$$

for the best fit in a least squares sense.

The response coefficients for each location in the gulf are estimated from the corresponding time series of data. Each temperature time series $T_s(x, t_j)$ is first detrended to remove any seasonal or linear trends. Missing data in each image were estimated by fitting the available data to the first five gradient EOF modes and reconstructing the SST from the estimated amplitudes and spatial mean (see equation (7)).
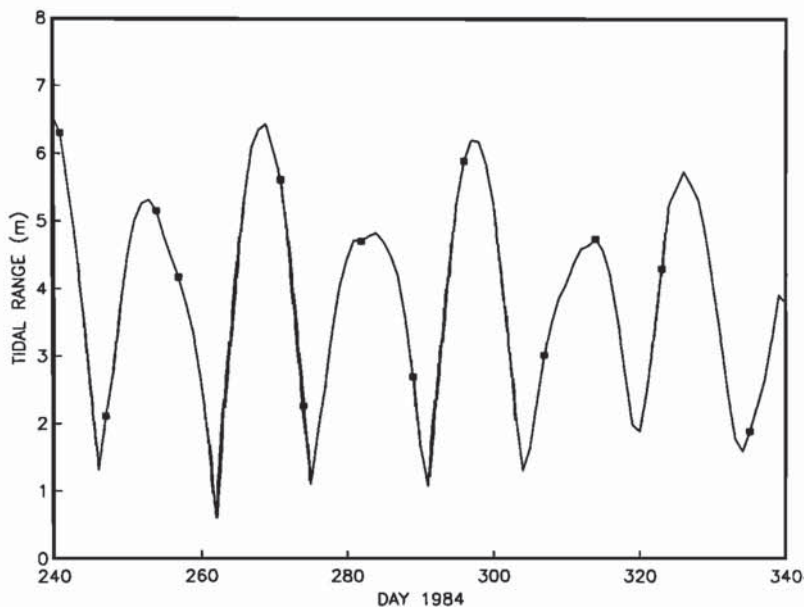

Fig. 19. Distribution of images used in linear statistical model relative to phase of the spring-neap tide. The solid line shows variation in tidal range, and squares indicate days for which relatively clear satellite images were available.
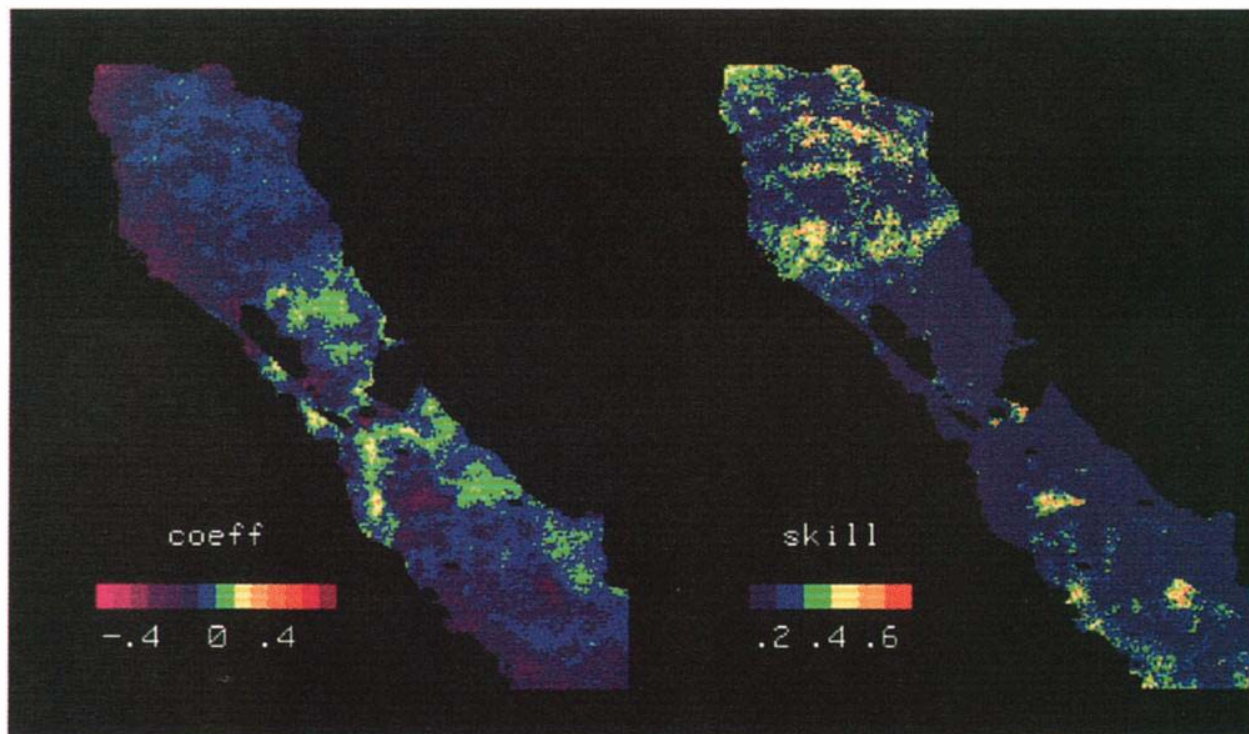
Plate 3. (a) Spatial distribution of the coefficients for the linear statistical model of SST as a function of tidal range in the northern Gulf of California. (b) Spatial distribution of the skill or percent variance explained by the linear statistical model.

The response coefficients are presented as an image in Plate 3, along with the estimated skill of prediction. The skill is that portion of the total SST variance which can be explained by variations in the tidal range. The skill is low over much of the northern gulf, which for the most part is simply a reflection of the fact that direct tidal forcing is limited to a few specific regions. However, some areas where tidal mixing is expected to occur also have low skill, while areas where we would least expect strong tidal mixing have high predictive skill. This type of result stems from the use of such a small number of irregularly spaced images in which missing data also need to be estimated. However, the distribution of the model coefficients, particularly those with large amplitudes, can tell us something about the relative response of the various regions to tidal forcing.

The model coefficients are generally negative and small in amplitude except for a few regions where the values are between -0.3 and -0.5. In these regions temperatures vary as much as 1°C solely as a result of tidal mixing. Large negative coefficients are present on the shallow northern shelf, over San Esteban Sill, in Tiburon Channel, over the sill in Ballenas Channel, at the northern tip of the island of Angel de la Guarda, and along the shallow ridge connecting the islands of Angel de la Guarda and San Lorenzo. Some indication of tidal mixing is also seen at the southern tip of San Lorenzo Island as well as along the top of the sill which runs south from there.

Each of the aforementioned regions is predicted to be vertically well mixed by the h/u^3 criterion of Simpson and Hunter [1974] [Argote et al., 1985; M. L. Argote, personal communication, 1990]. This criterion attempts to differentiate well-mixed regions from those which are stratified by assessing the potential energy balance for the water column. What is interesting to note here is that these regions show significant changes in SST over the spring-neap tidal cycle, suggesting that the water column is not completely mixed throughout that time. Although there is a qualitative agreement between the h/u^3 model and the distribution of the statistical model coefficients, there are regions that appear to respond to the tides which are not indicated by the h/u^3 criterion. Note the relatively large spot of negative values southeast of the islands. This area is approximately 600 m deep and has currents of much lower amplitude than those observed in the channels. The apparent response of the surface temperature to tidal forcing is therefore somewhat surprising. This area overlies a bathymetric spur which continues south from the islands and is believed to be a site of internal wave generation. Expendable bathythermograph (XBT) temperature profiles taken near the ridge during spring tide showed the presence of stair step structures over much of the water column [Paden and Hendershott, 1986]. Other regions in the Guaymas Basin with relatively large response coefficients have not been studied in situ, so it is difficult to ascertain whether the apparent correlation is reasonable.

Positive coefficients are present throughout much of the island region. These correlations appear to result from the advection of SST fronts by the tides (see Figure 2). The band of positive coefficients south of the islands (green band in Plate 3) corresponds to the position of a strong temperature front between the cold waters of the island region and the warmer waters of the Guaymas Basin. The positive coefficients in the statistical analysis indicate that the front moves towards the sill region during spring tide, bringing warm
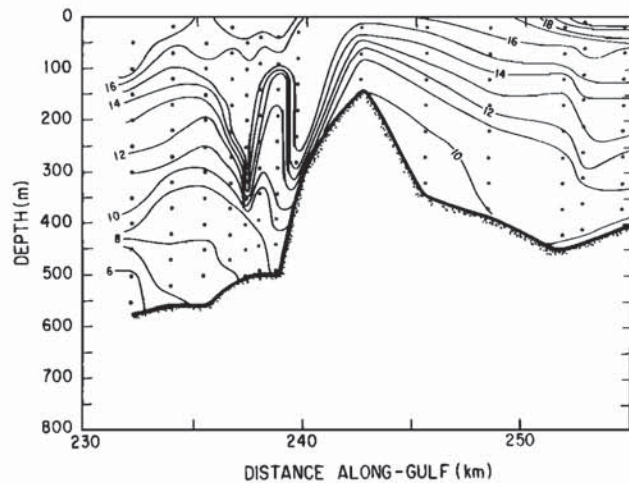
Fig. 20. XBT temperature section across San Esteban Sill during spring tides. Currents flowing south (to the left in figure). Distance is in kilometers along the gulf axis from 27°N, 111°W.

waters into the area. During neap tides the reverse occurs, and the cold waters of the island region advance into the Guaymas Basin. The width of the feature is approximately 10–15 km and is indicative of the frontal displacement over the spring-neap tidal cycle. This motion is counter to what might be expected for tidal mixing front regimes in which the horizontal extent of the well-mixed water would increase as tidal currents intensify. Here, advection rather than vertical mixing appears to be important in the displacement of the front. Estimates of along-channel geostrophic velocity fluctuations from near-surface bottom pressure measurements (C. A. Paden and C. D. Winant, unpublished data, 1984–1985) show a spring-neap modulation of the mean southward surface flow during fall and winter with an apparent decrease in the mean flow during spring tides and an increase during neaps. These observations are consistent with observations made at sills in Puget Sound [Geyer and Cannon, 1982] and the Strait of Gibralter [Candela et al., 1989] where increased baroclinic flow is observed during the neap tidal cycle.

In situ observations of tidal mixing. Much of the mixing and tidal energy dissipation in the northern gulf can be attributed to bottom friction. However, in the channels, significant SST variability at the tidal frequency is observed where bottom depths are of the order of several hundred meters. During a hydrographic cruise in November 1984, an XBT section [Paden and Hendershott, 1986] was made through the cold SST anomaly over San Esteban Sill to examine the vertical temperature structure (Figure 20). The contoured isotherms suggest the presence of an internal hydraulic jump or large breaking internal wave in the lee of the sill during spring falling tides. A conductivity-temperature-depth (CTD) cast made in the lee of the sill (Figure 21) shows density inversions indicative of strong vertical mixing in the upper 300–500 m [Bray et al., 1986]. This mixing facilitates the introduction of cold, deep Guaymas Basin water (8°C) into the surface mixed layer. Similar isotherm displacements have also been observed in the Ballenas Channel (M. C. Hendershott, unpublished data, 1983) where another cold SST anomaly exists. Hydraulic jumps presumably form when the fluid velocity u exceeds the speed c of a low-mode tidal-frequency internal wave

(i.e., when the Froude number squared is greater than 1; $F^2 = u^2/c^2 > 1$). Although the sill regions are predicted to be tidally well mixed by the h/u^3 model, the dynamics of the flow over the sills is much different than that used in deriving the tidal mixing parameter. The fact that the observed fluctuations in SST are consistent with the h/u^3 model may actually reflect similarities in the spatial distribution of the Froude number.

5.3. Wind Forcing

The SST pattern described by gradient mode 2 (Plate 2) resembles the general cooling which occurs near Tiburon Island when winds are upwelling favorable for the eastern side of the gulf (Figures 3 and 23). During these periods, cold water originating near the southern tip of Tiburon Island appears to be advected across the gulf toward the Baja peninsula as well as being entrained into a plume to the southeast. Similar plumes have also been observed in association with capes and headlands along the California coast during periods of upwelling-favorable winds [Brink et al., 1984; Kelly, 1985].

The short-time-scale behavior of gradient mode 2 (Figure 12) is not significantly different from that observed for the monthly mean images (Figure 8). A comparison of the estimated amplitudes for gradient mode 2 to the along-gulf winds at Tortuga Island (Figure 22) shows a correlation in the seasonal signals but very little if any short time-scale response. This would be expected, since the pattern is also dependent on the times scales of advection and horizontal eddy diffusivity. Some suggestion of a response on intermediate time scales appears evident around days 240 and 400 when reversals or large decreases in the along-gulf wind are reflected in the sign and magnitude of the EOF amplitudes.

A comparison of the image from November 9, 1984 (Figure 3) with one on November 18, 1984 (Figure 23) suggests that the cold water upwelled near Tiburon is entrained into the anticyclonic basin circulation. This water appears to be advected along the slope where it is mixed with shelf water before leaving the coast as a cold plume of water. Measurements on the Guaymas shelf are consistent with these observations with a correlation between low-frequency temperatures and currents seen only on a seasonal time scale [Merrifield and Winant, 1989]. Evidence of upwelling can also be seen along the coast near a small island to the north of Guaymas and off the headland south of Guaymas Bay. These upwelling plumes are small compared to that generated at Tiburon and would have much less influence on the large-scale temperature field in the Guaymas Basin. The cooler waters generated by the upwelling at Tiburon also appear to be advected across the gulf along the northern rim of the Guaymas Basin, producing the large region of cold SSTs apparent in the gradient mode 2 pattern.

In the spring and summer, shelf temperatures along the northern and eastern coasts of the gulf are warmer than those along the Baja California peninsula. Summertime images, however, show no obvious signs of upwelling along the Baja coast, and cooler waters previously observed south of the islands [Badan-Dangon et al., 1985] may in fact result from the advection of tidally mixed waters from the north. During the summer, the surface circulation in the Guaymas Basin is generally cyclonic (Figure 6). Water from the island region could be advected downcoast and then appear as a

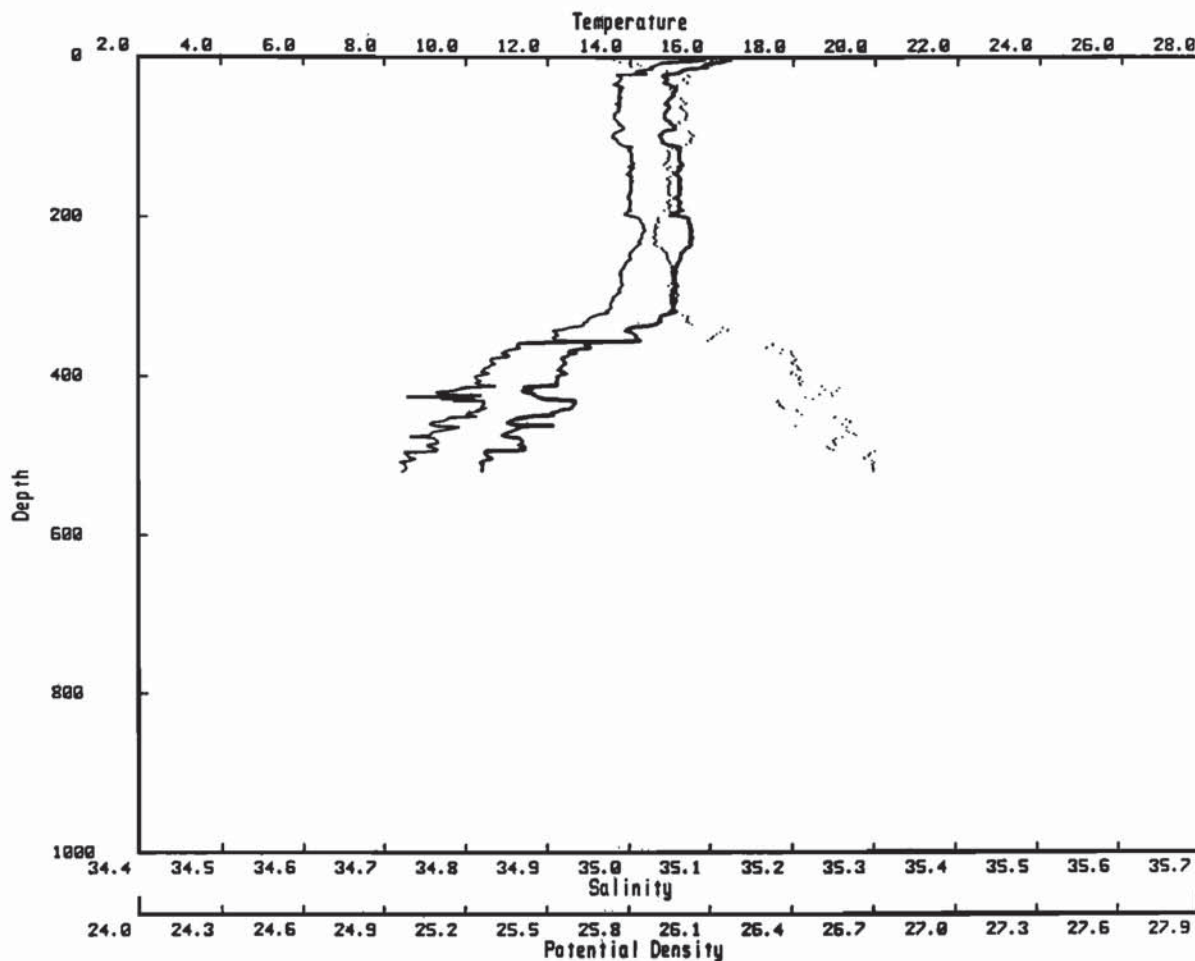STATION PC6100 :   28   37.0 N   112   39.0 W   24/11/84   1458Z   520/ 526m

Fig. 21. Vertical profiles of temperature, salinity, and potential density from a CTD cast made in the lee of San Esteban Sill during spring tides. Temperature (in degrees Celsius) is shown by the bold line, salinity (practical salinity units) is shown by the light solid line, and potential density is shown by the dotted line [*Bray et al.*, 1986].

plume near Santa Rosalia when it is entrained into the large-scale circulation. The influx of tidally mixed water along the western side of the gulf could also explain the temperature differences observed between the two shelves during the spring and summer. The possibility of upwelling along the Baja California coast cannot be eliminated, however, since not enough satellite data were available to examine the SST response to upwelling-favorable winds.

On the northern shelf, SSTs covary with the cooler temperatures produced in the fall and winter by upwelling off Tiburon Island. This occurs because the winds which are upwelling favorable along the Mexican mainland are also very cold when first blowing off the continent [*Badan-Dangon et al.*, 1991]. When the seasonal winds first reverse in the fall, the northern shelf is quite warm. The large difference in the air-sea temperature as well as the low humidity of the continental air mass would result in large losses of heat from the ocean near the coast. Tidal mixing on the shallow shelf also contributes to the cooling of sea surface during the fall and explains the patterns observed in the Colorado River delta in gradient mode 2.

6. SUMMARY AND DISCUSSION

Tidal mixing is the dominant mechanism by which the large-scale sea surface temperature patterns are established in the northern Gulf of California. Resonant to the semidiurnal tide, the northern gulf attains large tidal ranges which result in significant current velocities when constrained to flow through the narrow channels and over the relatively shallow sills of the island region. The sills separate deep waters of the northern basin and Guaymas Basin and are the generation sites for internal hydraulic jumps which mix water over depths of 300–500 m. This mixing introduces deep, cold Guaymas Basin water into the surface layer, producing the persistent pool of cold water evident in the mean SST field as well as in mode 1 of the gradient EOF analysis. The temporal behavior of this mode on short times scales suggests that the large-scale SST patterns are produced when cold temperatures generated at the sills by the tides are mixed horizontally.

A statistical model of the SSTs in the gulf as a function of tidal range shows that tidal mixing occurs over the shallow
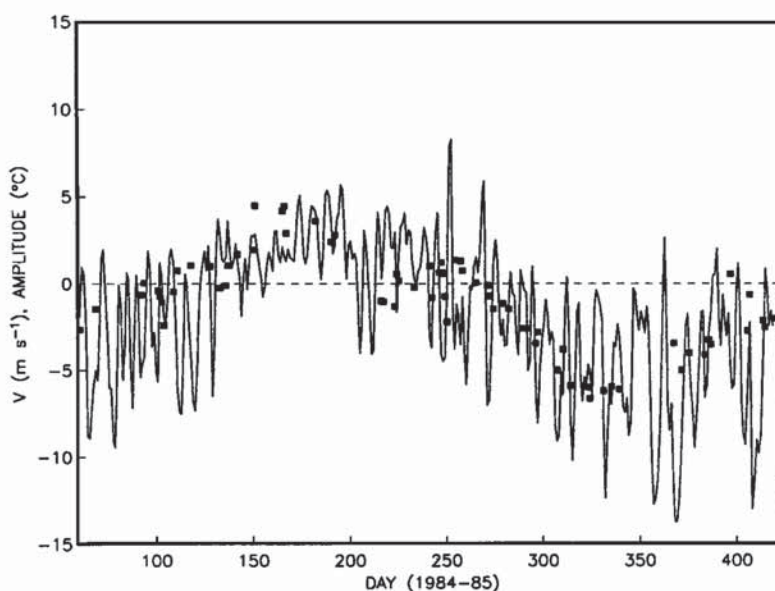
Fig. 22. Comparison of the estimated amplitudes for gradient mode 2 for individual images between March 1, 1984, and February 28, 1985, and the low-frequency along-gulf winds at Tortuga Island.

northern shelf as well as at the sills. Tidal mixing on the shelves, however, occurs in depths of less than 60 m compared with 500 m at the sills. The deeper mixing results in the production of much colder SSTs and establishes spatial patterns which are different from those seen in other tidal mixing regimes, where the coldest temperatures occur in shallow water near the coast [*Simpson and Hunter*, 1974; *Loder and Greenberg*, 1986]. Comparison of the statistical model results to estimates of h/u^3 for the Gulf of California [*Argote et al.*, 1985; M. L. Argote, personal communication, 1989] reveals a qualitative agreement for most of the island region and northern basin. However, additional regions of tidal mixing are apparent in the satellite analysis, especially

Fig. 23. AVHRR image for November 18, 1984 showing entrainment of upwelling plume into anticyclonic basin circulation.

in the Guaymas Basin. The mixing at the sills occurs primarily as a result of hydraulic jumps which are not properly modeled by the tidal mixing parameter h/u^3, which is derived using bottom friction. The agreement between the observations and the distribution of the h/u^3 parameter may result from a similarity in the distribution of the Froude number which predicts the location and occurrence of the hydraulic jumps. The discrepancy in the type of mixing also shows up in the behavior of a temperature front located south of the islands. In the statistical analysis it was evident from the distribution of the coefficients that this front moved closer to the area of strong tidal mixing during spring tides and further away during neap tides. This behavior is opposite to that expected for tidal mixing fronts, where the region of well-mixed water expands with the increased tidal velocities moving the front into the region which was previously well stratified. The displacement of the front was related instead to spring-neap variations in the surface mean flow.

Cool temperatures generated by tidal mixing at the sills appear to be mixed horizontally over much of the northern basin. To the south, the cold water does not appear to have as great an influence on the Guaymas Basin except perhaps along the Baja California coast. This behavior suggests the importance of the large-scale circulation in the maintenance of the SST patterns. Hydrographic observations indicate that the surface circulation in the Gulf of California is cyclonic during the summer with a weaker, anticyclonic circulation during the rest of the year [*Bray*, 1988a]. SST patterns evident in mode 1 of the covariance EOF analysis are consistent with the observed circulation for the northern basin. Relatively warm SSTs are present over the shallow northern shelf during the summer with a minimum in SST over the Delphin Basin. During winter the shallow shelves are much cooler than the gyre center, consistent with the anticyclonic circulation during that time of year. The SST gradients appear to be stronger during summer, when hydrographic measurements show the largest geostrophic currents [*Bray*, 1988a]. These relationships suggest that the temper-

ature gradients established by the differential heating and cooling of the shelves may be the driving mechanism for the gyre circulation in the northern basin. A corresponding gyre pattern, however, is not apparent in the Guaymas Basin SSTs even though the circulation is similar to that observed in the northern basin. This large-scale circulation would maintain cool waters throughout the northern basin due to the entrainment of the tidally mixed waters from the island region. In the Guaymas Basin, SSTs remain warmer owing to advection of water from the southern gulf which is not influenced by tidal mixing.

The differential behavior of the shelf region is evident in the second mode of both the covariance and gradient EOF analyses. During the spring and early summer, shelf temperatures are warmer than offshore, while during late fall and early winter they are much colder. Much of this behavior is explainable in terms of tidal mixing. However, during winter the shelf region cools in response to the wind field. The winds in the gulf are monsoonal, blowing from the southeast during the summer and out of the northwest during the rest of the year. During winter the winds bring cool, dry air from off the continent. This air mass would result in a large heat loss on the northern shelf, where temperatures are initially quite warm. These same winds are also upwelling favorable along the Mexican mainland, accounting for the covariability of cool temperatures off Tiburon Island with those over the shallow northern shelf. Additional upwelling is also evident near small capes and headlands further south but is not as extensive. The cold water upwelled at Tiburon is entrained in the anticyclonic circulation in the Guaymas Basin. This cool water can be seen along the shelf slope south of Tiburon Island, where it appears to mix with water on the shelf before leaving the coast near Guaymas. During spring and summer, the broad northern and eastern shelves are warmer than the rest of the gulf. Although some evidence of upwelling on the western side of the gulf has been observed near Santa Rosalia [*Badan-Dangon et al.*, 1985], the cooler temperatures there may instead result from the advection of tidally mixed waters south along the coast of Baja.

The northern Gulf of California is also strongly forced by the atmosphere. Spatially averaged temperatures for the northern basin, island region, and Guaymas Basin exhibit similar temporal variability, with large fluctuations predominantly in the spring and early summer. These fluctuations in the SST were associated with similar changes in the air temperature which occurred in response to synoptic weather events. Increased winds from the north and sometimes the south bring cooler air over the gulf. In low-wind conditions, the warm desert air extends over the ocean and SSTs increase. During these periods, warm SST anomalies were visible in the satellite data. The areal extent of these features was related to the length of the warming period. Discrepancies between aircraft measurements and satellite-derived SSTs suggest that these features are the result of intense surface heating which occurs when wind speeds are particularly low.

The dominant influence of tidal mixing on the SST, as well as on water mass formation processes, points to its key role in the net gain of heat by the Gulf of California. The Mediterranean and Red seas, both of which lose heat to the atmosphere, do not have significant tides. Vigorous tidal mixing in the gulf pumps heat deep into the water column, thereby maintaining the cooler SSTs. These SSTs are then dispersed over much of the northern gulf through advection and horizontal mixing and have a large impact on the exchange of heat by lowering the saturation vapor pressure of the air. This would reduce the amount of heat lost to the atmosphere through evaporation and explain the discrepancy between earlier surface heat flux estimates from coastal meteorological data [*Roden and Emilsson*, 1979] and those inferred from the advective heat transport [*Bray*, 1988a]. Atmospheric estimates made from the coast would not take into account the cool SSTs produced offshore by tidal mixing. Hydrographic estimates of the freshwater flux [*Bray*, 1988a] indicated a reduction in the latent or evaporative heat flux of nearly one half over that obtained from coastal meteorological data. When this value for the latent heat flux was combined with atmospheric estimates of the other fluxes, the net surface heat flux became positive into the ocean in agreement with the hydrographic results.

REFERENCES

Alvarez-Borrego, S., Gulf of California, in *Estuaries and Enclosed Seas*, edited by B. H. Ketchum, pp. 427–449, Elsevier, New York, 1983.

Argote, M. L., A. Amador, and C. Morales, Variación estacional de la estratificacíon en la región norte del Golfo de California, in *Memorias de la Reunión Anual 1985*, edited by J. Urrutia-Fucugauchi and J. F. Valdés-Galicia, pp. 334–338, Unión Geofísica Mexicana, Mexico City, 1985.

Badan-Dangon, A., C. J. Koblinsky, and T. Baumgartner, Spring and summer in the Gulf of California: Observations of surface thermal patterns, *Oceanol. Acta, 8*, 13–22, 1985.

Badan-Dangon, A., C. Dorman, M. A. Merrifield, and C. D Winant, The lower atmosphere over the Gulf of California, *J. Geophys. Res.*, in press, 1991.

Bray, N. A., Thermohaline circulation in the Gulf of California, *J. Geophys. Res..*, 93(C5), 4993–5020, 1988a.

Bray, N. A., Water mass formation in the Gulf of California, *J. Geophys. Res.*, 93(C8), 9223–9240, 1988b.

Bray, N. A., M. C. Hendershott, J. M. Robles, and A. C. Carrasco, Pichicuco 6: Gulf of California CTD data report, November, 1984, *SIO Ref. 86-5*, 1986. Scripps Inst. of Oceanogr., La Jolla, Calif., 1986.

Brink, K. H., D. W. Stuart, and J. C. Van Leer, Observations of the coastal upwelling region near 34°30'N off California: Spring 1981, *J. Phys. Oceanogr., 14*, 378–391, 1984.

Bunker, A. F., H. Charnock, and R. A. Goldsmith, A note on the heat balance of the Mediterranean and Red seas, *J. Mar. Res., 40*, suppl., 73–84, 1982.

Candela, J., A. Badan-Dangon, and C. D. Winant, Spatial distribution of lower atmospheric physical variables over the Gulf of California, A data report, vol. 2: Winter 1984, *SIO Ref. 85-11*, Scripps Inst. of Oceanogr., La Jolla, Calif., 1985.

Candela, J., C. D. Winant, and H. L. Bryden, Meteorologically

forced subinertial flows through the Strait of Gibraltar, *J. Geophys. Res.*, *94*(C9), 12,667–12,679, 1989.

Cornillon, P., and L. Stramma, The distribution of diurnal warming events in the western Sargasso Sea, *J. Geophys. Res.*, *90*(C6), 11,811–11,815, 1985.

Davis, R. E., Predictability of sea surface temperature and sea level pressure anomalies over the North Pacific Ocean, *J. Phys. Oceanogr.*, *6*, 249–266, 1976.

Filloux, J. H., Tidal patterns and energy balance in the Gulf of California, *Nature*, *243*, 217–221, 1973.

Flament P., L. Armi, and L. Washburn, The evolving structure of an upwelling filament, *J. Geophys. Res.*, *90*(C6), 11,765–11,778, 1985.

Fu, L.-L., and B. Holt, Internal waves in the Gulf of California: Observations from a spaceborne radar, *J. Geophys Res.*, *89*(C2), 2053–2060, 1984.

Geyer, W. R., and G. A. Cannon, Sill processes related to deep water renewal in a fjord, *J. Geophys. Res.*, *87*(C10), 7985–7996, 1982.

Hendershott, M. C., and A. Speranza, Co-oscillating tides in long, narrow bays: The Taylor problem revisited, *Deep Sea Res.*, *18*, 959–980, 1971.

Kelly, K. A., The influence of winds and topography on the sea surface temperature patterns over the northern California slope, *J. Geophys. Res.*, *90*(C11), 11,783–11,798, 1985.

Kelly, K. A., Comment on "Empirical orthogonal function analysis of advanced very high resolution radiometer surface temperature patterns in Santa Barbara Channel" by G. S. E. Lagerloef and R. L. Bernstein, *J. Geophys. Res.*, *93*(C12), 15,753–15,754, 1988.

Kelly, K. A., and R. E. Davis, An analysis of errors in sea surface temperature in a series of infrared images from NOAA 6, *J. Geophys. Res.*, *91*, 2633–2644, 1986.

Lagerloef, G. S. E., and R. L. Bernstein, Empirical orthogonal function analysis of advanced very high resolution radiometer surface temperature patterns in Santa Barbara Channel, *J. Geophys. Res.*, *93*(C6), 6863–6873, 1988.

Lavin, M. F., and S. Organista, Surface heat flux in the northern Gulf of California, *J. Geophys Res.*, *93*(C11), 14,033–14,038, 1988.

Loder, J. H., and D. A. Greenberg, Predicted positions of tidal fronts in the Gulf of Maine region, *Cont. Shelf Res.* *6*(C3), 397–414, 1986.

McClain, E. P., W. G. Pichel, and C. C. Walton, Comparative performance of AVHRR-based multichannel sea surface temperatures, *J. Geophys. Res.*, *90*(C6), 11,587–11,601, 1985.

Merrifield, M. A., and C. D. Winant, Shelf circulation in the Gulf of California: A description of the variability, *J. Geophys. Res.*, *94*(C12), 18,133–18,160, 1989.

Paden, C. A., and M. C. Hendershott, Observations of temperature finestructure in the Gulf of California: XBT data report, November 1984/March 1985, *SIO Ref. 86-14*, Scripps Inst. of Oceanogr., La Jolla, Calif., 1986.

Roden, G. I., Oceanographic and meteorological aspects of the Gulf of California, *Pac Sci.*, *12*(1), 21–45, 1958.

Roden, G. I., Oceanographic aspects of the Gulf of California, in *Marine Geology of the Gulf of California: A Symposium, Mem. Am. Assoc. Pet. Geol. 3*, edited by T. H Van Andel and G. G. Shor, Jr., pp. 30–58, American Association of Petroleum Geologists, Tulsa, Okla., 1964.

Roden, G. I., and I. Emilsson, Physical oceanography of the Gulf of California, paper presented at the Gulf of California Symposium, in Commemoration of the 50th Anniversary of the Universidad Nacional Autónoma de Mexico, Univ. Nac. Autom. de Mex., Mexico City, 1979.

Roden, G. I., and G. W. Groves, Recent oceanographic observations in the Gulf of California, *J. Mar. Res.*, *18*, 10–35, 1959.

Simpson, J. H., and J. R. Hunter, Fronts in the Irish Sea, *Nature*, *250*, 404–406, 1974.

Stock, G. G. Modelling of tides and tidal dissipation in the Gulf of California, Ph.D. thesis, 102 pp., Scripps Inst. of Oceanogr., Univ. of Calif., San Diego, 1976.

Universidad Nacional Autónoma de Mexico, Tablas de predicción de mareas, 1970, Anales del Instituto de Geofísica, vol. 15, Apendice I, Parte B, Dep. de Oceanogr., Inst. de Geofis., Mexico City, 1969.

M. R. Abbott and C. A. Paden, College of Oceanography, Oceanography Administration Building 104, University of Oregon, Corvallis, OR 97331.

C. D. Winant, Center for Coastal Studies, 0209, Scripps Institution of Oceanography, La Jolla, CA 92093.